Fossil oceanic core complexes in the Alps. New field, geochemical and isotopic constraints from the Tethyan Aiguilles Rouges Ophiolite (Val d'Hérens, Western Alps, Switzerland)

Thierry Decrausaz, Othmar Müntener, Paola Manzotti, Romain Lafay, Carl Spandler

Decrausaz *et al. Swiss J Geosci* (2021) 114:3
https://doi.org/10.1186/s00015-020-00380-4

SGG SGS sc | nat
Swiss Journal of Geosciences

ORIGINAL PAPER Open Access

Fossil oceanic core complexes in the Alps. New field, geochemical and isotopic constraints from the Tethyan Aiguilles Rouges Ophiolite (Val d'Hérens, Western Alps, Switzerland)

Thierry Decrausaz[1,2*], Othmar Müntener[1], Paola Manzotti[3], Romain Lafay[2] and Carl Spandler[4]

Abstract

Exhumation of basement rocks on the seafloor is a worldwide feature along passive continental margins and (ultra-) slow-spreading environments, documented by dredging, drilling or direct observations by diving expeditions. Complementary observations from exhumed ophiolites in the Alps allow for a better understanding of the underlying processes. The Aiguilles Rouges ophiolitic units (Val d'Hérens, Switzerland) are composed of kilometre-scale remnants of laterally segmented oceanic lithosphere only weakly affected by Alpine metamorphism (greenschist facies, Raman thermometry on graphite: 370–380 °C) and deformation. Geometries and basement-cover sequences comparable to the ones recognized in actual (ultra-) slow-spreading environments were observed, involving exhumed serpentinized and carbonatized peridotites, gabbros, pillow basalts and tectono-sedimentary cover rocks. One remarkable feature is the presence of a kilometric gabbroic complex displaying preserved magmatic minerals, textures and crosscutting relationships between the host gabbro and intruding diabase, hornblende-bearing dikelets or plagiogranite. The bulk major and trace element chemistry of mafic rocks is typical of N-MORB magmatism (Ce_N/Yb_N: 0.42–1.15). This is supported by in-situ isotopic signatures of magmatic zircons ($\varepsilon Hf = +13 \pm 0.6$) and apatites ($\varepsilon Nd = +8.5 \pm 0.8$), determined for gabbros and plagiogranites. In-situ U–Pb dating was performed on zircons by laser ablation-ICP-MS, providing ages of 154.9 ± 2.6 Ma and 155.5 ± 2.8 Ma, which are among the youngest for oceanic gabbros in the Alps. Our study suggests that the former Aiguilles Rouges domain was characterized by tectonism and magmatism resembling present-day (ultra-) slow-spreading seafloor. It also suggests that the Tethyan lithosphere is laterally segmented, with punctuated magmatism such as the Aiguilles Rouges gabbros and carbonated ultramafic seafloor covered by basalts and Jurassic tectono-sedimentary deposits.

Keywords: Alpine Tethys, Ophiolites, Oceanic core complex, MORB magmatism, Geochronology, Zircon, Apatite

1 Introduction

Over the last decades, various types of spreading systems (Dick et al. 2003) have been identified worldwide, highlighting diverse modes for the generation of oceanic crust that depend on mantle potential temperature, mantle fertility and spreading rate. The "layered" ophiolite sequence, proposed as a type model of oceanic crust (Penrose Conference, Anonymous 1972), closely matches for observations and sequences derived from fast-spreading environments such as the Samail ophiolite (Glennie et al. 1974; Hopson et al. 1981; Nicolas and Boudier 1995), or the Troodos ophiolite (Moores and Vine 1971). However, investigations along present-day (ultra-) slow-spreading environments provided evidence of a more

Editorial handling: Stefan Schmid.

*Correspondence: thierry.decrausaz@gm.univ-montp2.fr
[1] Institute of Earth Sciences, University of Lausanne, Géopolis, Quartier Mouline, 1015 Lausanne, Switzerland
Full list of author information is available at the end of the article

complex formation and evolution of the oceanic lithosphere that is quite different from the Penrose definition. One major difference is the exposure of serpentinized peridotites and gabbros at the seafloor (i) along transform settings (e.g. Miyashiro et al. 1969; Bonatti and Honnorez 1976), (ii) at or close to mid-ocean ridges (e.g. Karson 1990; Cannat 1993; Tucholke and Lin 1994; Cannat et al. 1995; Dick et al. 2000, 2003), and (iii) along passive continental margins (Boillot et al. 1980; Lagabrielle and Auzende 1982). Along (ultra-) slow-spreading ridges, the magmatic crust is segmented and discontinuous, as plate separation is accommodated by both magmatism and tectonic stretch (e.g. Cannat et al. 1997; Karson and Lawrence 1997). This combination is documented by the formation of oceanic core complexes (OCCs) located at or near the spreading axis (e.g. Cann et al. 1997; Tucholke et al. 1998; Nicolas et al. 1999; MacLeod et al. 2002; Cannat et al. 2006; Smith et al. 2006). OCCs are domed edifices consisting of exhumed peridotite and gabbros that form the footwall of long-lived detachment faults (e.g. Cann et al. 1997; Tucholke et al. 1998; MacLeod et al. 2009). The latter may root at shallow depth or at the brittle-ductile transition of the lithosphere (Tucholke et al. 1998, 2008; Escartin et al. 2003). They accommodate most of the deformation during magma-starved periods but the mechanisms triggering the initiation of faulting still remain unclear. From numerical modelling, OCCs may develop by the interplay of plate extension by magmatism and tectonism (Shemenda and Grocholsky 1994; Buck et al. 2005; Tucholke et al. 2008) and develop into a flip-flop mode of extension for magma-poor periods (Reston and McDermott 2011; Gillard et al. 2015; Bickert et al. 2020). During such magma-starved extensional deformation, trapping of mantle-derived magmas is expressed by: (i) the emplacement of large gabbroic intrusions (Ildefonse et al. 2007), (ii) the absence of effusive products onto active slip surfaces (MacLeod et al. 2009), and (iii) the formation of corrugation structures (MacLeod et al. 2002).

It has long been recognized that Alpine ophiolites are different from what has later become the Penrose type ophiolites (e.g. Decandia and Elter 1969; Bonatti 1971). These and subsequent work paved the way to understand modern (ultra-) slow-spreading environments. Field data revealed comparable geometries and basement-cover sequences in many Tethyan ophiolites (e.g. Lombardo and Pognante 1982; Tricart and Lemoine 1983; Lagabrielle 1994; Manatschal et al. 2011; Balestro et al. 2015; Festa et al. 2015; Lagabrielle et al. 2015; Tartarotti et al. 2017); all these examples being similar to the Central Atlantic, as envisioned by Lagabrielle and Cannat (1990). However, an important extension of our understanding of ophiolites formed in (ultra-) slow-spreading systems within orogens is that some ophiolitic units were identified as representing ancient ocean-continent transition zones (OCT) now preserved in the Eastern Central Alps and Northern Apennines (Florineth and Froitzheim 1994; Molli 1996; Müntener and Hermann 1996; Manatschal and Nievergelt 1997; Epin et al. 2019).

A unifying element of both interpretations is the type and age of oceanic magmatism. Gabbros and basalts of mid-Jurassic ages have been found in almost all ophiolite remnants in the Alps, but their volumes are small and they show a remarkable diversity ranging from olivine-rich troctolites to Mg-gabbros to Fe–Ti–rich hornblende gabbros and plagiogranites (e.g. Lombardo et al. 2002; Tribuzio et al. 2016), regardless of later Alpine metamorphic overprint. In most places, they intrude as dikes into mantle rocks and, locally, they form 10 to 100's of metre-sized bodies with internal intrusive relationships (e.g. Desmurs et al. 2002; Sanfilippo and Tribuzio 2013), testifying for limited melt supply during the formation of the Alpine Tethyan lithosphere. Kilometre-sized gabbroic bodies in Alpine ophiolites are not common and are mostly overprinted by high-pressure metamorphism (e.g. Lagabrielle et al. 2015; Festa et al. 2015); however, their magmatic construction is poorly constrained.

In this paper, we first provide evidence for a MOR type gabbro (the Aiguilles Rouges d'Arolla Gabbro) within the Tsaté nappe in the Western Alps that has largely escaped Alpine deformation. The Tsaté nappe, formerly interpreted as a tectonic wedge (Marthaler and Stampfli 1989), provides evidence of mantle denuded at the seafloor, intruded by gabbros and, locally, directly overlain by Jurassic sediments. This evidence is based on field observations and a petrological and isotope geochemical study of gabbroic rocks and associated basalts. We use these data to show that the Aiguilles Rouges d'Arolla Gabbro is derived from magmas similar to those of ultra-slow spreading mid-ocean ridges and represents the youngest large volume gabbroic body within the Alps with a crystallization age of ~155 Ma. In-situ Hf-isotopes of zircon and in-situ Nd isotopes of apatite confirm a source similar to modern MORB for the Aiguilles Rouges Gabbro. We develop a conceptual model of core complex formation for the Aiguilles Rouges Gabbro and infer that exhumed mantle sequences and large gabbroic bodies may form part of the axial domains of Tethyan lithosphere.

2 Geological setting

2.1 Piemonte-Liguria ocean

Alpine ophiolites are lithospheric fragments inherited from the Alpine Tethys (hereafter referred to as Piemonte-Liguria ocean), a former oceanic basin resulting from rifting followed by seafloor spreading between the

European and Adriatic plates (e.g. Bernoulli and Jenkyns 1974; Trümpy 1975; Lemoine 1985; Stampfli et al. 1998; Schmid et al. 2004; Handy et al. 2010; Manzotti et al. 2014). Seafloor spreading was already active in the Bajocian, as sustained by: (i) the dating of post-rift pelagic sedimentary rocks deposited onto oceanic crust lithologies (Elter et al. 1966; Bill et al. 2001), and (ii) U–Pb dating of zircon-bearing mafic rocks related to the onset of crustal accretion (Manatschal and Müntener 2009; Tribuzio et al. 2016; Renna et al. 2017). Late Cretaceous Alpine convergence led to the emplacement of oceanic material in the Alpine nappe stack (e.g. Stampfli and Marthaler 1990; Stampfli et al. 1998; Molli 2008).

2.2 The Aiguilles Rouges ophiolites in the Tsaté nappe

Units derived from the Piemonte-Liguria ocean are mainly exposed in the Western and Central Alps. The Tsaté nappe (Sartori 1987) is a unit derived from the Piemonte-Liguria ocean that crops out in north-western Italy and southern Switzerland (Valais), between the underlying Grand-Saint-Bernard and the overlying Dent Blanche nappes (Fig. 1). It consists of calcareous and terrigenous metasediments, most probably Jurassic to Cretaceous in age (e.g. Marthaler 1984), and minor ophiolites (e.g. Witzig 1948; Hagen 1948; Bugnon and Haarpaintner 1979; Marthaler 1984; Kunz 1988; Allimann 1990). Marthaler and Stampfli (1989) interpreted the Tsaté nappe as a tectonic wedge developed during subduction of the Piemonte-Liguria ocean.

In the Val d'Hérens (Valais, Western Swiss Alps), the Tsaté nappe has been subdivided in two main different units, the Série Grise and the Aiguilles Rouges d'Arolla Zone (Witzig 1948; Kunz 1988; Marthaler and Stampfli 1989). However, the tectonic contacts between these two units have not been traced on any regional geological map. The Série Grise, an equivalent of the Schistes Lustrés complex (Marthaler and Stampfli 1989; Deville et al. 1992), is essentially composed of quartz-rich calcschists, alternating with levels of marble and mafic material (Marthaler 1984; Sartori 1987). The presence of radiolarites at the Col des Ignes (Witzig 1948; Hagen 1948) points towards a Jurassic age for pelagic sediments associated with oceanic crust lithologies, while the discovery of planktonic foraminiferas (Rotalipora) within the sediments of the Série Grise inferred an Upper Cretaceous (Cenomanian) age to this flysch-type deposit (Marthaler 1984). The Série Grise is overlain by the Aiguilles Rouges d'Arolla Zone, which gathers discontinuous ophiolites at the Aiguilles Rouges d'Arolla and further north in the Val d'Arolla. The latter zone exposes dismembered kilometre-scale tectonic slivers of gabbro, basalt and serpentinized peridotite, located beneath the contact with the Dent Blanche nappe (Fig. 2).

In the Série Grise and the Aiguilles Rouges ophiolites, Alpine metamorphism reached upper greenschist facies conditions, with its typical paragenesis of epidote + actinolite/tremolite + chlorite + albite + titanite in the mafic rocks and rare sodic amphibole (e.g. riebeckite in the metamorphosed pillow-lavas from the Mont des Ritses;

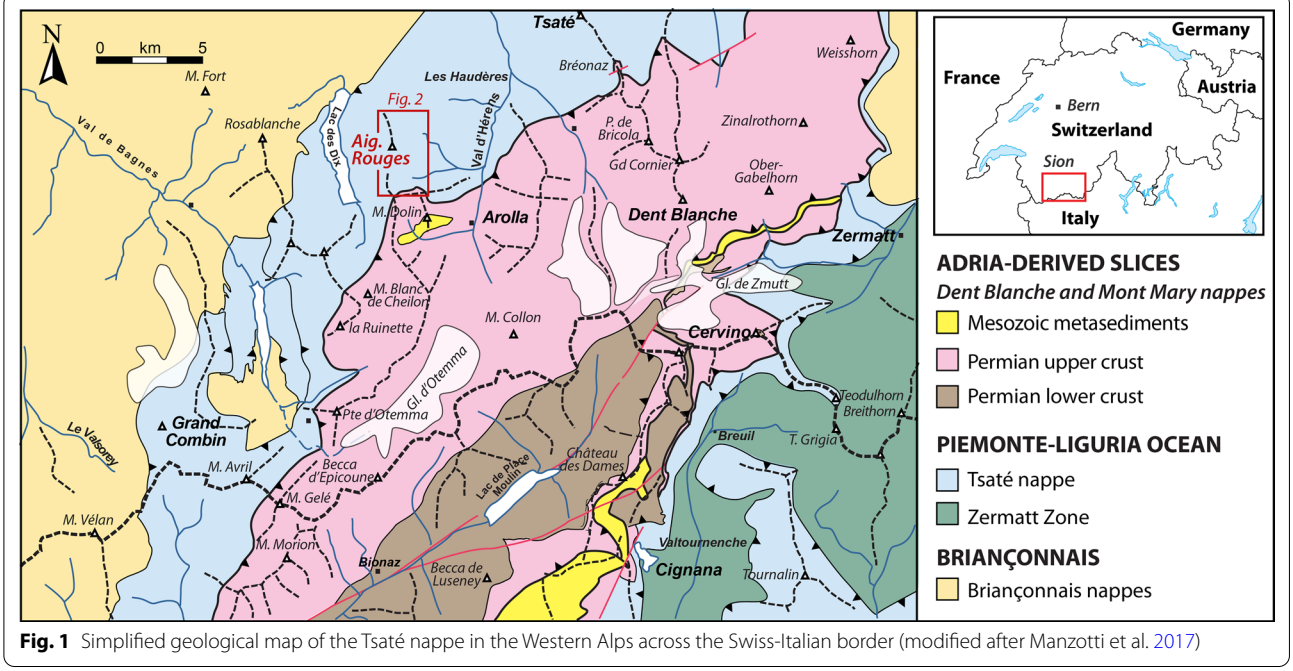

Fig. 1 Simplified geological map of the Tsaté nappe in the Western Alps across the Swiss-Italian border (modified after Manzotti et al. 2017)

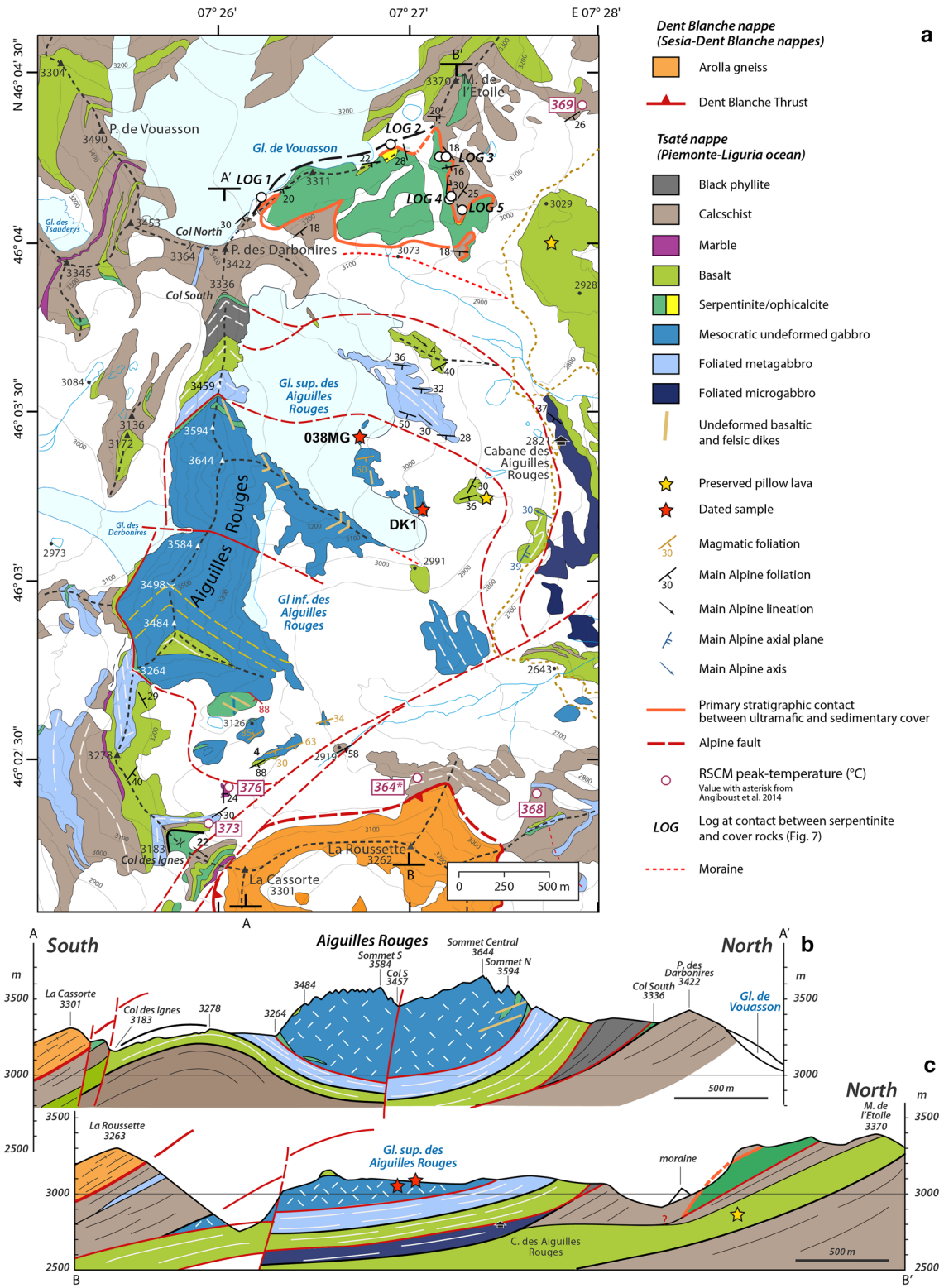

Fig. 2 **a** Geological map of the Aiguilles Rouges area, modified after Marthaler (2010) and Girard (2012). Coordinate system is WGS84. **b** Cross-section between La Cassorte and Pointe des Darbonires. **c** Cross-section between La Roussette and Mont de l'Etoile. Both cross-sections show the geometry of the main lithologies in the Aiguilles Rouges area

Angiboust et al. 2014). Raman spectroscopy on carbonaceous materials provided temperatures of 360–400 °C for calcschists exposed close to the contact with the Dent Blanche nappe (Angiboust et al. 2014). No barometric estimations have been provided for the Aiguilles Rouges d'Arolla Zone.

3 Methodology

3.1 Raman spectroscopy on carbonaceous material (RSCM)

Raman spectra were obtained at the University of Lausanne, with a HR Raman-FTIR spectrometer from HORIBA Scientific, an integrated Raman microprobe consisting of an Olympus BX41 confocal microscope coupled to an 800 mm focal-length spectrograph. A 532.12 nm frequency-doubled Nd-YAG continuous-wave laser was focused on the sample and the laser power at the sample surface was 19 mW. The Raman signal was collected in backscattered mode. The sampled volume was a few μm^3 using a $100\times$ objective. Acquisition time for measurements was 6×20 s. Spectra were recorded using the software LabspecTM v. 4.14. The spectrometer was calibrated with a silicon standard before each session. Because Raman spectroscopy of carbonaceous materials (CM) can be affected by several analytical mismatches, we followed closely the analytical procedures described by Beyssac et al. (2002, 2003). Measurements were carried out on polished thin sections and CM was analysed below a transparent adjacent mineral, generally quartz. 10 to 22 spectra were recorded for each sample in the extended scanning mode (1000–2000 cm^{-1} with acquisition times of 120 s). Spectra were then processed using the software Peakfit (Beyssac et al. 2003).

The serpentine polymorphs have been characterized by Raman spectroscopy coupled with petrographic observations of polished thin-sections. The acquisition of the reflected Raman signal was accumulated for 120 s in two cycles, with a laser power at the sample surface of approximately 700 μW. A reproducibility of 1 cm^{-1} was attained on successive spectra of a given mineral sample. The spectral regions from 150 to 1150 cm^{-1} and from 3600 to 3720 cm^{-1} were investigated because they include the lattice vibrational modes and the OH stretching mode region that is characteristic of serpentine species (e.g. Groppo et al. 2006).

3.2 Bulk rock chemistry

Bulk rock samples were crushed and powdered using an agate mill, except for serpentinized peridotites (tungsten mill). The powders were dried in a furnace at 105 °C overnight. Loss on ignition (LOI) was determined after heating ca. 2.5 g of powder per sample in a muffle furnace at 1050 °C for 90 min. The ignited powders (1.2 g ± 0.0002) were mixed with lithium tetraborate (6 g ± 0.0002), and then homogenized using an agate mortar and pestle. The mixtures were fused twice in platinum-gold crucibles at 1250 °C for 3 min, then quenched to produce homogeneous glass beads for analysis. Bulk major element concentrations were measured on lithium tetraborate glasses by X-Ray fluorescence (XRF), using a PANalytical AxiosmAX spectrometer at the University of Lausanne. Standards BHVO, NIM-G, NIM-N, SY-2, UB-N2 were used for internal quality control (Additional file 1).

Bulk trace element compositions were measured on the flat side of broken pieces of glasses using an Agilent 7700 quadrupole inductively coupled plasma mass spectrometer, interfaced to a GeoLas 200M ArF excimer ablation system at the University of Lausanne. He and Ar were used as carrier gases. The ablation spot diameter was 150 μm. For glasses from mafic and ultramafic rocks, the on-sample energy density was set at 6.0 J/cm^2 and the repetition rate at 10 Hz. For the plagiogranite, those values were modified to 8.0 J/cm^2 and 20 Hz respectively. Three repeat measurements were performed for each sample, except for the glass from the plagiogranite (two analyses). Acquisition times for the background and laser ablation signals were 90 and 45 s. Two standards (SRM 612 from NIST) were measured at the beginning and at the end of each serie of analysis to correct for drift of the instrument. The blank concentration was determined before each ablation and the associated spectrum was subtracted from the analyte. The absolute trace element concentrations were determined by processing the data with the program Lotus 1-2-3 release 5.01 and the spreadsheet LAMTRACE (Longerich et al. 1996; Jackson 2008). The CaO content obtained from XRF analysis was used as an internal standard, except for samples presenting contents < 5 wt% (typically serpentinites). In that case, the XRF SiO_2 content was used. The trace element quantification was elaborated using the preferred values from the external standard SRM 612 from NIST (Pearce et al. 1997).

3.3 U–Pb geochronology

Zircon crystals from two samples (038MG and DK1) were separated using standard magnetic and heavy liquid mineral separation techniques at the University of Lausanne. Grains of similar size were handpicked and mounted on 25 mm epoxy pucks, and polished to expose grain centers. The internal structure of zircon was investigated by cathodoluminescence (CL) imaging, using a CamScanMV2300 scanning electron microscope at the University of Lausanne. U–Pb ages of zircon were obtained on Thermo Scientific Element XR coupled to a New Wave ArF 193 nm laser at the University of Lausanne, following the methods of Ulianov et al.

(2012). The spot diameter was set to 35 µm, but eventually reduced to 25 µm with on-sample energy density of 3.0 J/cm^2 and a repetition rate of 5 Hz. The instrument mass bias was calibrated by 40 measurements of zircon reference material GJ-1 (CA-TIMS $^{206}Pb/^{238}U$ age of 600.5 ± 0.4 Ma; Boekhout et al. 2012), yielding a mean $^{206}Pb/^{238}U$ ratio of 0.09760 ± 0.00045. The calibration was controlled by 10 measurements of Plešovice zircon, which was used as secondary standard ($^{206}Pb/^{238}U$ age of 337.12 ± 0.37 Ma; Sláma et al. 2008); 10 analyses yielded a mean of 337.86 ± 2.70 Ma. The raw data were computed using the program Lotus 1-2-3 release 5.01 and the applications CONGEOFF and LAM-UPb (Jackson 2008). The corrected ratios and calculated $^{206}Pb/^{238}U$ ages are presented in Additional file 1: Table S4 and standard analysis are presented in Additional file 1. U–Pb normal Concordia and weighted mean age diagrams are calculated using Isoplot 3.75 (Ludwig 2012).

3.4 Chemistry of zircon

In-situ trace element composition of zircon was measured on the same mounts selected for dating. The measurements were performed on the Element XR, coupled to a NewWave UP-193 ArF excimer ablation system with conditions as described above for dating. Ba, Rb and Sr contents were monitored during the analysis to track the ablation of inclusions or fractures. The output data were computed using the application LAMTRACE (Longerich et al. 1996). A stoichiometric value of SiO_2 content (32.1 wt%) was used for signal quantification.

3.5 Hf isotopes of zircon

In-situ Hf isotope analysis by laser ablation MC-ICPMS employed a Neptune Plus at the University of Geneva, coupled to a Photon Machines "Analyte G2" 193 nm laser ablation system connected to a HelEx II two-volume cell. Ablation was performed at a fluence of 6.5 J/cm^2, a repetition rate of 5 Hz and an ablation spot size of 35 µm. Helium is introduced directly into the cell, with addition of a small flow of nitrogen to the sample gas upstream of the cell to increase sensitivity. Analytical blanks were measured after every ~10 analyses by collecting data without ablating. No systematic drift in blank values was observed. Further details of the analytical protocol are described in Ewing et al. (2019).

The following isotopic ratios were determined by LA-ICP-MS: $^{179}Hf/^{177}Hf$, $^{178}Hf/^{177}Hf$, $^{171}Yb/^{173}Yb$, $^{174}Hf/^{177}Hf$, $^{176}Lu/^{177}Hf$ and $^{176}Hf/^{177}Hf$. The zircon grains were ablated on the same domains selected for U–Pb dating. The data were extracted from the software Evaluation of the Neptune Plus. The data were corrected for isobaric interferences and mass bias, using the Lu and Hf isotopes ratios of Thirlwall and Anczkiewicz (2004) and a value of 0.786945 for the $^{176}Yb/^{173}Yb$ ratio. The corrected data are provided in Additional file 1: Table S5 for the $^{176}Lu/^{177}Hf$ and $^{176}Hf/^{177}Hf$ ratios. The $^{176}Hf/^{177}Hf_{CHUR}$ initial ratio, involved in the determination of the εHf, was calculated using present time values of 0.282785 for the$^{176}Hf/^{177}Hf_{CHUR}$ ratio and 0.0336 for the $^{176}Lu/^{177}Hf_{CHUR}$ ratio (Bouvier et al. 2008). The measurement of the 4 internal standards (MUN, GJ-1, Mud Tank, Plesovice) provided low average offset values ranging between 0.1 and 0.3, and associated standard deviations comprised 0.2 and 0.5 (Additional file 1: Table 5): The low analytical errors on the standards guarantee the accuracy of the measurements on zircon for both samples. The initial $^{176}Hf/^{177}Hf_{CHUR}$ and $^{176}Lu/^{177}Hf_{CHUR}$ ratios were calculated using previously determined U–Pb ages (Additional file 1).

3.6 Sm–Nd isotopes of apatite

In-situ Sm–Nd isotopic analyses of apatite from two gabbro samples (038MG and DK1) were carried out at the Advanced Analytical Centre, James Cook University, Townsville, Australia, using a ThermoScientific NEPTUNE multicollector ICP-MS coupled to the Photon Machines Analyte G2 193 nm laser ablation system. Ablation was carried out in a HelEx II two-volume ablation cell with He used as the aerosol transport gas. Details of the multicollector set-up are presented in Hammerli et al. (2014). In-situ laser ablation analyses were acquired over 60 s with a pulse rate of 4 Hz, a laser energy density at the sample site of 3 J/cm^2 and ablation pit diameters of between 85 and 130 µm. Interference and mass bias corrections were made according to the method of Fisher et al. (2011). The $^{147}Sm/^{144}Nd$ ratios were derived by calibration to a synthetic LREE-rich silicate glass ($^{147}Sm/^{144}Nd = 0.2451$; Fisher et al. 2011), which was routinely analysed throughout the analytical session. Apatite $^{143}Nd/^{144}Nd$ ratios were further normalized to bracketing analyses of Nd-doped glass (JNdi-1, TIMS $^{143}Nd/^{144}Nd = 0.512098 \pm 13$; Fisher et al. 2011). The normalization factors for $^{147}Sm/^{144}Nd$ and $^{143}Nd/^{144}Nd$ ratios were ~0.5% and 12 ppm, respectively.

Three secondary mineral standards were analysed as quality control measures: Otter Lake and Durango apatites (Fisher et al. 2011; Yang et al. 2014), and MKED1 titanite (Spandler et al. 2016). Our initial $^{143}Nd/^{144}Nd$ results for Otter Lake (n = 6) of 0.511430 ± 8 (2SD), agree well with in-situ LA-ICP-MS values reported by Yang et al. (2014) of 0.511447 ± 45 (2SD). Our analyses of Durango apatite (n = 3) gave initial $^{143}Nd/^{144}Nd$ values of 0.512436 ± 32 (2SD), which is in good agreement with the ratios acquired by LA-MC-ICP-MS reported by Fisher et al. (2011) (0.512463 ± 48), Hammerli et al. (2014) (0.512468 ± 39) and Yang et al. (2014)

(0.512472 ± 46), and the TIMS value of 0.512489 ± 12 (Fisher et al. 2011). Analyses of MKED1 titanite (n = 3) returned initial $^{143}Nd/^{144}Nd$ values of 0.510382 ± 27 (2SD), which is also with uncertainty of the TIMS reference value of 0.510363 ± 5 (2SD) (Spandler et al. 2016).

4 Field relationships

The studied area covers approximately 20 km^2 including the Aiguilles Rouges massif and extending from the northern end of the Dent Blanche nappe to the Mont de l'Etoile (Fig. 2). Here the Tsaté nappe comprises several tectonic slices made of mafics, ultramafics, and metasediments. The Alpine metamorphism is generally low, whereas Alpine deformation is heterogeneous. A few low strain domains preserved primary magmatic and basement-cover relationships, whereas other areas are affected by intense Alpine deformation. Spectacular examples are the two main ophiolitic complexes, the Aiguilles Rouges Ophiolite and the Mont de l'Etoile Ophiolite. By contrast, intense Alpine deformation can be observed in the Col des Ignes and Pointe des Darbonires areas (Fig. 2), where deformation mainly localized in metasediments. The main features of the Aiguilles Rouges and Mont de l'Etoile Ophiolites and the Col des Ignes-Pointe des Darbonires areas are described below.

4.1 The Aiguilles Rouges Ophiolite

The Aiguilles Rouges Ophiolite comprises a kilometre-scale tectonic slice of undeformed and weakly metamorphosed gabbro, associated with minor serpentinized peridotites and metabasalts. Serpentinized peridotites occur at the bottom of the Aiguilles Rouges Gabbro, on its northern and southern side. They are located structurally below the main gabbro body and the metabasalts. The recent snow retreat has exposed a large amount of serpentinite at the foot of the cliffs, close to a newly formed lake at les Ignes. Serpentinized peridotite is crosscut by gabbroic dikes, which are themselves cut by basaltic rocks and an anastomozing network of carbonate veins (Fig. 3).

The undeformed mesocratic *gabbro* (hereafter called Aiguilles Rouges Gabbro) mainly constitutes the Aiguilles Rouges peaks (Fig. 2). The Aiguilles Rouges Gabbro typically displays a phaneritic texture with centimetre-scale clinopyroxene bordered by black amphibole and pseudomorphs after plagioclase (Fig. 4a, b). Magmatic clinopyroxene is partially replaced by acicular actinolite/tremolite and chlorite (Fig. 6c–c'). Hornblende replaces exsolution lamellae of the former pyroxene (Fig. 6a–a') or form as magmatic interstitial grains. Magmatic plagioclase recrystallized into a fine-grained assemblage of albite, chlorite and epidote.

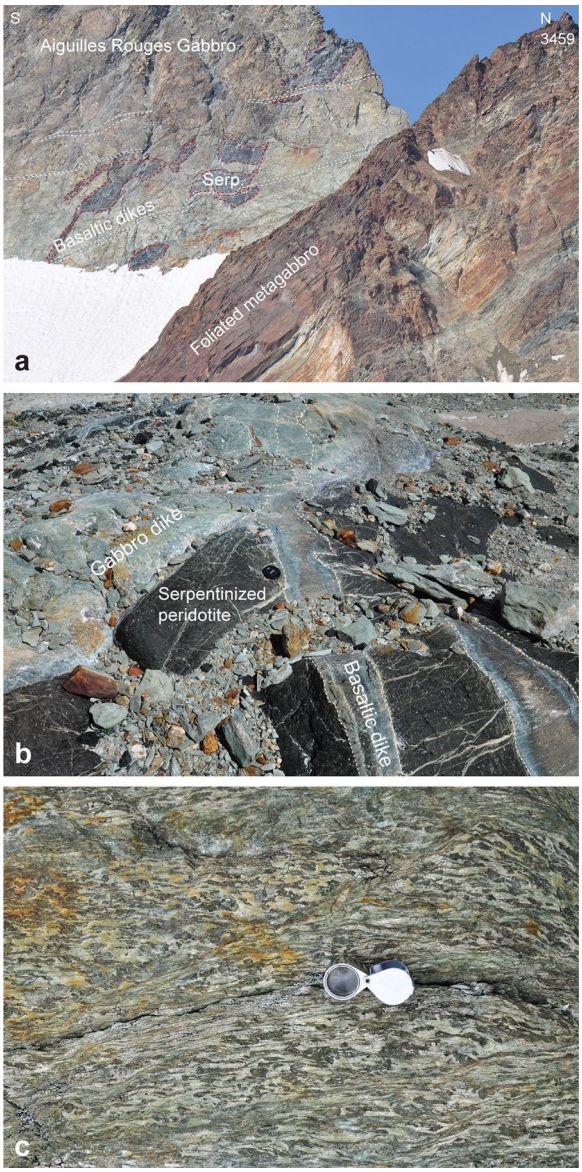

Fig. 3 Field aspects of the Aiguilles Rouges massif. **a** Lenses of ultramafic rocks at the northern end of the Aiguilles Rouges Gabbro are cut by basaltic dikes. **b** Serpentinized harzburgite cut by a gabbro dike. The gabbro dike is cut by basaltic dikes. Note that basaltic dikes developed chlorite blackwalls in contact with serpentinized harzburgite. The lens cover diameter is 8 cm. (Coordinates: N46°02′36.04″, E7°26′01.36″). **c** Deformed Aiguilles Rouges gabbros with mm-scale high temperature mylonitic shear zones. The handlens is 6 cm long)

Accessory phases, idiomorphic zircon and acicular or idiomorphic apatite aggregates, are generally found as interstitial phases between the former clinopyroxene and plagioclase.

On the southern side of the Aiguilles Rouges Gabbro, a steep, south dipping high-temperature foliation was

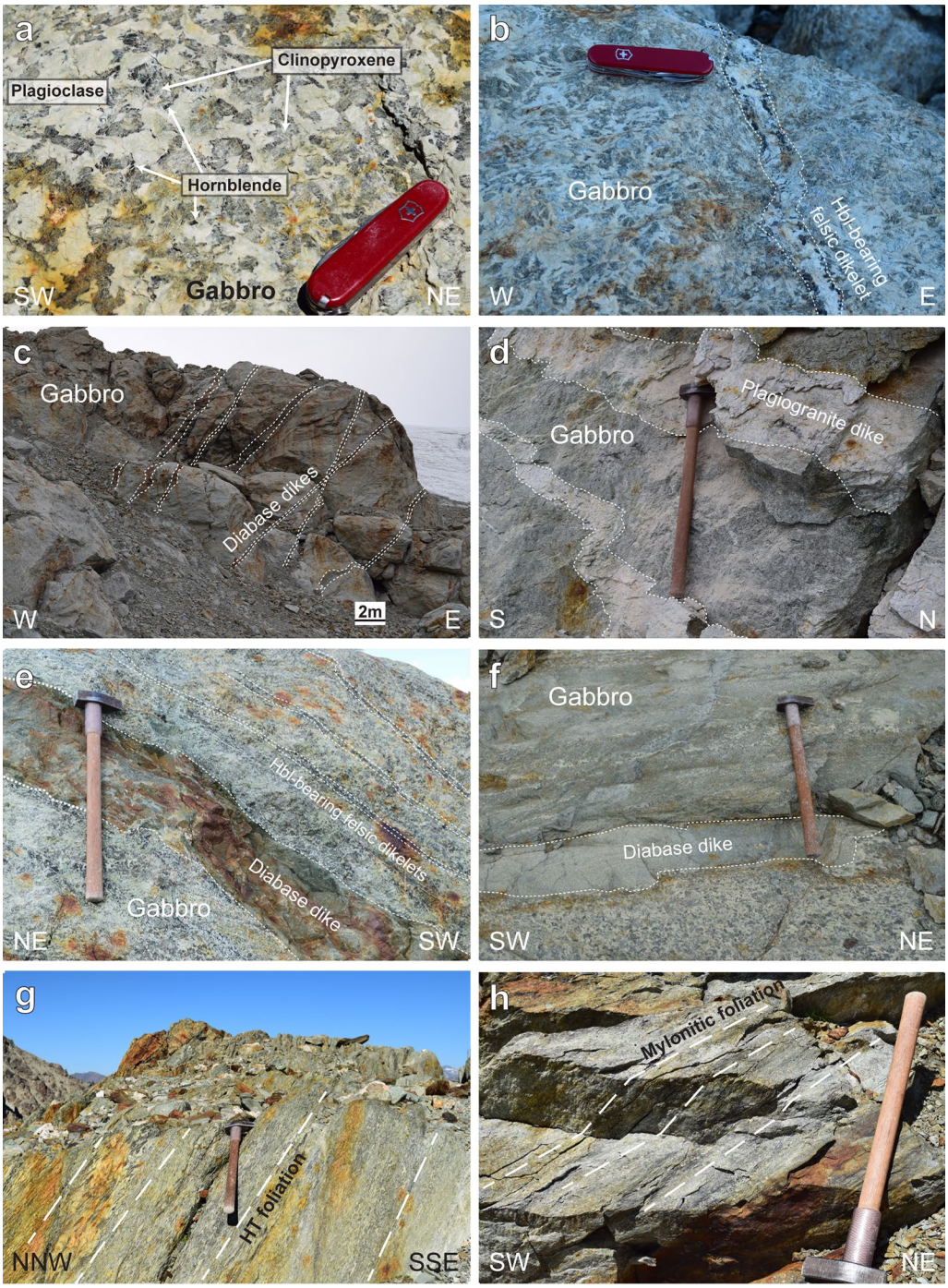

Fig. 4 Field aspects of the Aiguilles Rouges Gabbro. Photographs captured below the Glacier Supérieur des Aiguilles Rouges (**a**–**e**), at Les Ignes (**f**, **g**) and on the eastern slopes of the Aiguilles Rouges peaks (**h**). **a** Undeformed mesocratic gabbro displaying a magmatic phaneritic texture composed of a matrix of metamorphosed plagioclase and clinopyroxene grains bordered by black interstitial amphibole. **b** Undeformed mesocratic gabbro cut by a horblende-bearing felsic dikelet. **c** Diabase dikes crosscutting the undeformed Aiguilles Rouges gabbro. **d** Plagiogranite dikes intruding the Aiguilles Rouges gabbro and exhibiting syn-magmatic deformation. **e** Diabase and hornblende-bearing felsic dikelets intruding gabbro. **f** Undeformed mesocratic gabbro exhibiting magmatic heterogeneities and grain-size variations and crosscut a by diabase with a preserved microgabbroic texture. **g** Metagabbro exhibiting high-temperature ductile deformation, marked by the alignment of metamorphosed pyroxene and hornblende. **h** Metagabbro overprinted by Alpine mylonitic deformation

observed, marked by the alignment of the former clinopyroxene and hornblende (Fig. 4g).

The Aiguilles Rouges Gabbro is intruded by swarms of *diabase dikes*, *hornblende-bearing felsic dikelets* and a few *plagiogranite dikes* (Fig. 4b, c, e). *Diabase* intruding the Aiguilles Rouges Gabbro can be observed in the eastern side of the Aiguilles Rouges peaks. They form greyish-brownish 0.3 to 2 m thick dike swarms (Fig. 4c). Dikes form planar structures extending over 10 s of metres. They dip to the NW at high-angle (Fig. 4c), and cut the high-temperature foliation of the gabbros. Diabase is completely altered and only one dike was observed to show remnants of a magmatic texture (Fig. 4f). Diabase dikes show greenschist-facies assemblages composed of fined-grained epidote, albite, minor chlorite and rare actinolite/tremolite. Diabase shows sharp contacts with the gabbros. Backveining structures are observed and thin veins of albite frequently cut across edges of the dikes. At les Ignes, diabase dikes intruding serpentinized peridotites are metasomatically altered, with chlorite blackwalls at the contact (Figs. 3, 5). In this area, dikes are subvertical and oriented NS and EW. Within serpentinites, diabase is essentially composed of chlorite, apatite and oxides with no relic of the primary magmatic minerals. East–west oriented dikes are partially replaced by carbonates.

Hornblende-bearing felsic dikes are ubiquitous and form a network of centimetre-thick veins cutting the main Aiguilles Rouges Gabbro (Fig. 4b, e). These dikes and diabase exhibit similar orientations and were not observed to cut each other. These small dikes consist of fine-grained plagioclase cores and are bordered by centimetric subhedral to euhedral brown hornblende; however, some dikelets are hornblende-rich. Hornblende shows a reddish-brownish colour typical of igneous amphibole (Fig. 6d). Fractures crosscutting the hornblende grains are filled by chlorite or tremolite, and inclusions of former plagioclase are common. Apatite occurs as aggregates surrounding hornblende, as intergranular grains or as inclusions in hornblende (Fig. 6b, d). Ilmenite is associated with hornblende and apatite, as is typical for Fe–Ti gabbros (Fig. 6d), while zircon occurs as isolated subhedral grains (Fig. 6e). Plagioclase is completely replaced by a fine-grained assemblage of anhedral epidote and albite, along with minor chlorite and tremolite.

Rare, 0.1 to 0.3 m thick *plagiogranite* dikes were recognized within the Aiguilles Rouges Gabbro (Fig. 4d). The contacts between dikes and the host gabbros are sharp and planar, and exhibit syn-magmatic deformation. Plagiogranites are composed of anhedral plagioclase (sub- to plurimillimetric in size), along with minor hornblende, quartz, and accessory zircon and titanite. Margins of plagiogranite dikes are commonly rich in subhedral to euhedral hornblende. As in all other gabbroic units, plagioclase is partially replaced by epidote and albite, while hornblende is preserved or partially altered to chlorite + tremolite.

Metabasalts occur at the top and at the base of the Aiguilles Rouges peaks (on the southern and eastern sides, respectively; Fig. 2), but they are structurally above both the serpentinized peridotites and the main gabbro body. In the eastern side, massive metamorphosed basalts occur, suggesting their origin as massive lava flows. Primary magmatic structures such as pillow structures are found at the base of the Aiguilles Rouges peaks. Pillow lava structures are often elongated and flattened, of less than 1 m (Fig. 5a–c). Metabasalts exhibit (now filled) voids that may be interpreted as primary vesicles. The rocks display a typical yellowish-greenish colour, caused by the presence of metamorphic epidote, actinolite, chlorite and albite. Metabasalts display a fine-grained texture, with grain-size varying from the millimetre to the micrometre-scale. Pillow lava structures are also found north of the Cabanne des Aiguilles Rouges, in the Mont des Ritses area (Fig. 2).

To the North and to the East, the Aiguilles Rouges Ophiolite (Figs. 2 and 4h) is in tectonic contact with mylonitic metagabbros and metabasalts. These strongly deformed metagabbros are hornblende and oxide-rich, giving the rocks a typical reddish-purple weathering colour. Flaser-gabbros display a blastomylonitic texture with millimetre- to centimetre-scale elongated porphyroclasts of pyroxene and plagioclase. The latter is replaced by albite and surrounded by fine-grained chlorite, epidote, actinolite and albite marking an anastomosing foliation. Proto-mylonitic gabbros contain millimetre-thick mylonite bands and are composed of recrystallized porphyroblasts of albite and epidote supported by a matrix of cryptocrystalline epidote and albite, minor chlorite and rare tremolite/actinolite. In this area, due to the strong greenschist mylonitic deformation, the geological boundary with the mylonitized metabasalts remains uncertain. Diabase dikes were never observed crosscutting the mylonitic metagabbros. The mylonitized metabasalts, underlying the mylonitic metagabbros, display a banded texture, expressed by centimetre scale layers richer in epidote alternated to chlorite-rich layers.

4.2 The Mont de l'Etoile Ophiolite

The Mont de l'Etoile Ophiolite is located between the Pointe des Darbonires and the Mont de l'Etoile (Fig. 2) and preserves an exceptional primary basement-cover contact discontinuously exposed along ~ 1 km (Figs. 7, 8). In this area, five logs have been measured in order to investigate the basement-cover relationships. The basement consists of a kilometre-sized body of serpentinized

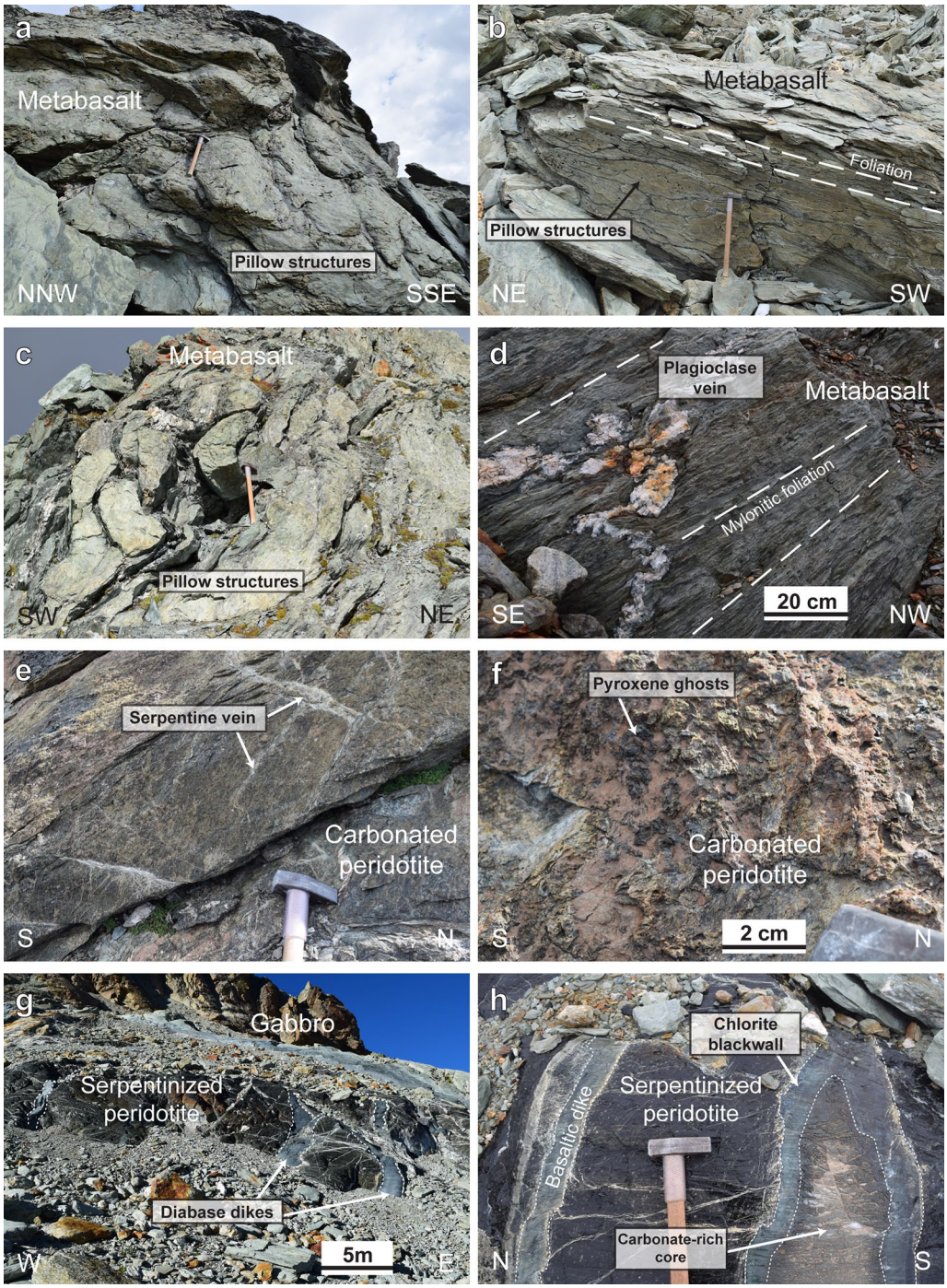

Fig. 5 Field aspects of metabasalts and serpentinized peridotites. Photographs were captured at the Mont de Ritses (**a**, **b**), in the Mont de l'Etoile area (**e**–**f**), on the eastern slopes of the Aiguilles Rouges peaks (**c**, **d**) and at les Ignes (**g**, **h**). **a**, **b** Flattened pillow metabasalts. **c** Weakly deformed pillow basalts. **d** Mylonitic metabasalt cut by plagioclase vein. **e** Carbonated serpentinized peridotite displaying serpentine veins. **f** Static carbonation of serpentinized peridotite, pyroxene ghosts can be recognized, the matrix is composed of serpentine and carbonate. **g** Metasomatized diabase dikes intruding serpentinized peridotite beneath the Aiguilles Rouges gabbro. **h** Metasomatized diabase dikes intruding serpentinized peridotite, their margins are chloritized while the inner part is carbonated

(See figure on next page.)

Fig. 6 Microphotographs of zircon-bearing samples 038MG (**a**–**c**) and DK1 (**d**, **e**). Plane-polarized light photographs on the left and crossed-polarized light on the right **a**–**a′** Clinopyroxene relic partially replaced by hornblende and bordered by apatite aggregates. **b**–**b′** Apatite + ilmenite aggregate found as interstitial phases between former pyroxene and metamorphosed plagioclase, replaced by epidote and albite. **c**–**c′** Idiomorphic zircon crystallized between cpx and (altered) plagioclase. **d**–**d′** Idiomorphic hornblende displaying double cleavages surrounded by altered plagioclase (fine-grained epidote + chlorite + albite). Hornblende contains apatite + ilmenite inclusions, **e**–**e′** Zircon + hornblende within a fine-grained epidote + chlorite + albite matrix

peridotites, intruded locally by diabase (Log 1) and a decametre-scale gabbroic body, whereas the cover is dominated by (Upper Jurassic ?) marble and calcschist with rare metabasalt (Log 1, Figs. 7b and 8a). Serpentinites do not contain any trace of primary mantle silicates, but relics of fresh Cr-spinel are preserved. Serpentinites are mostly massive exhibiting pseudomorphs of former orthopyroxene. They are composed of a dark-green homogeneous matrix containing bronzy bastite (Fig. 5h) and are crosscut by several generations of light green serpentine veins. Mesh texture, with mesh cores isolated by veinlets of serpentine containing magnetite droplets are common. Mesh cores are dominantly composed of antigorite with interstitial chrysotile as identified using Raman spectroscopy and interstitial veins are exclusively composed of antigorite. Serpentinites are commonly carbonated near the contact with the calcschists. Massive "blocky" serpentinite is progressively altered into talcschists close to the contact to sedimentary cover. Towards the contact with the cover, the ultramafic basement displays an increasing amount of brittle deformation, with massive "blocky" serpentinite passing to brecciated serpentinite and locally to serpentinite cataclasite (Log 1, Figs. 7b and 8a) or foliated serpentinite (Log 5, Figs. 7b and 8d). Millimetre- to centimetre-thick veins of chlorite or serpentine and calcite occur in the ultramafic basement, mainly oriented at high angle to the basement-cover contact. Ophicalcite has been observed at Logs 2 and 5 (Fig. 7b). This breccia is found in the uppermost level of exumed mantle, both in oceanic and ophiolitic settings (e.g. Lemoine 1967; Lemoine et al. 1987; Lagabrielle and Cannat 1990; Treves and Harper 1994; Vitale Brovarone et al. 2011; Meresse et al. 2012). In the Alps and Appennines, ophicalcite in comparable settings has been considered as evidence for exposure of ultramafic rocks at the seafloor. Locally, a 50–100-cm thick layer of talcschist is present on top of the basement (Logs 3 and 4), possibly documenting metasomatism of previous serpentinite. In Log 4, a metre-thick massive chlorite- and plagioclase-rich layer overlays the talcschist. The chemistry of this rock (sample L4-3, Additional file 1: Table S2) is compatible with a continental source. Tectono-sedimentary breccias, consisting of angular clasts of ultramafic rocks within a chlorite-rich matrix are observed directly on top of the deformed serpentinites or talcschist or the chlorite-, plagioclase-rich layer (Logs 2–5, Figs. 7b and 8b,c). Yellowish to whitish deformed marbles, with a thickness up to ~ 2 m, are observed on top of the breccias in correspondence of Logs 2 and 3 (Fig. 7b). Decametre-sized serpentinite clasts are locally found within the marble layer. These pelagic limestones are similar to marbles forming the basal levels of the sedimentary cover of several Alpine ophiolites (e.g. Lemoine et al. 1970; Lagabrielle et al. 1985; Ballèvre and Lagabrielle 1994). They are attributed to the Upper Jurassic (Tithonian) and are considered as a continuous layer ("Malm marbles") at the base of the Cretaceous metasedimentary series. They are comparable with the Calpionella limestone of Late Jurassic age forming the base of the sedimentary cover of the Appennine ophiolites (Lemoine 1971). Calcschists, with a thickness up to ~ 70 m are found on top of the breccias in correspondence of Logs 4–5. The contact between the ultramafic and the metasedimentary rocks is deformed (Fig. 2 and 4) with small folds that developed in the metasediments as result of the Alpine deformation.

4.3 Col des Ignes and Pointe des Darbonires areas

The Col des Ignes and the Pointe des Darbonires areas are both dominated by *metasedimentary rocks.* Rare metagabbros and metabasalts occur as decametric foliated slivers embedded within calcschists (e.g. on the eastern flank of La Roussette peak or at the Col des Darbonires; Fig. 2). In these areas, the metasedimentary rocks are mainly composed of (i) calcschists dominated by calcite, quartz, white micas and graphite, (ii) a few dm- to m-size blueish marble layers alternating with calcschist, and (iii) black phyllites. The well-pronounced bedding within calcschists is supported by the alternation between centimetre- to metre-size quartz- and carbonate-rich schists and marbles layers, and the presence of chlorite-rich layers and lenses. Raman spectroscopy on carbonaceous materials (RSCM) was conducted on four samples to determine the temperature recorded by the organic matter in calcschists following the method described by Beyssac et al. (2002). The maximum burial temperatures registered by the four samples are homogeneous with an average value of ca. 372 °C (± 20 °C) (Additional file 1: Table S7) in good agreement with data reported by Angiboust et al. (2014) for the same location.

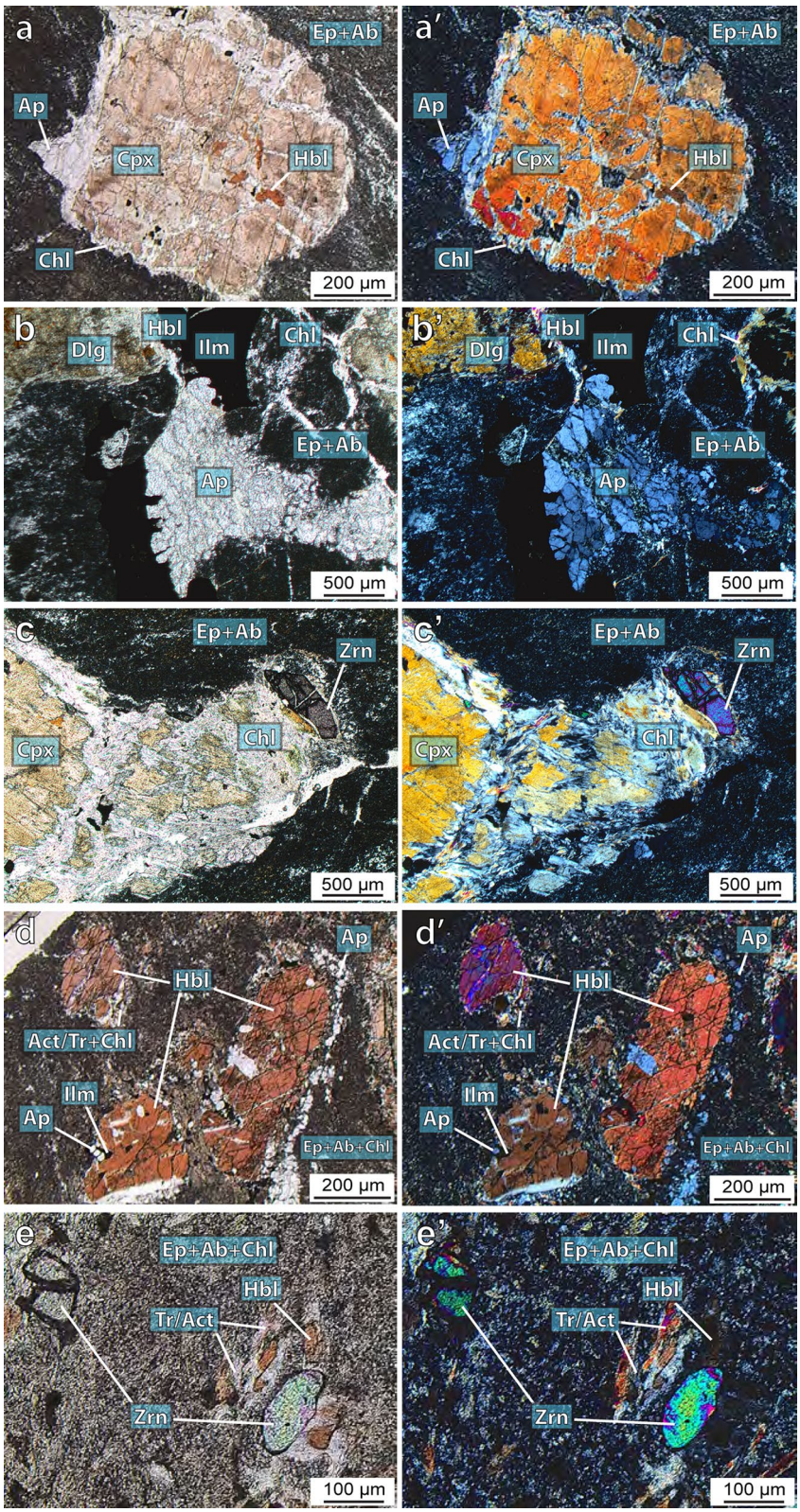
a
Ep+Ab
Ap
Cpx
Hbl
Chl
200 µm
a'
Ep+Ab
Ap
Cpx
Hbl
Chl
200 µm
b
Hbl
Dlg
Ilm
Chl
Ep+Ab
Ap
500 µm
b'
Hbl
Dlg
Ilm
Chl
Ep+Ab
Ap
500 µm
c
Ep+Ab
Zrn
Cpx
Chl
500 µm
c'
Ep+Ab
Zrn
Cpx
Chl
500 µm
d
Ap
Hbl
Act/Tr+Chl
Ilm
Ap
Ep+Ab+Chl
200 µm
d'
Ap
Hbl
Act/Tr+Chl
Ilm
Ap
Ep+Ab+Chl
200 µm
e
Ep+Ab+Chl
Hbl
Tr/Act
Zrn
100 µm
e'
Ep+Ab+Chl
Hbl
Tr/Act
Zrn
100 µm

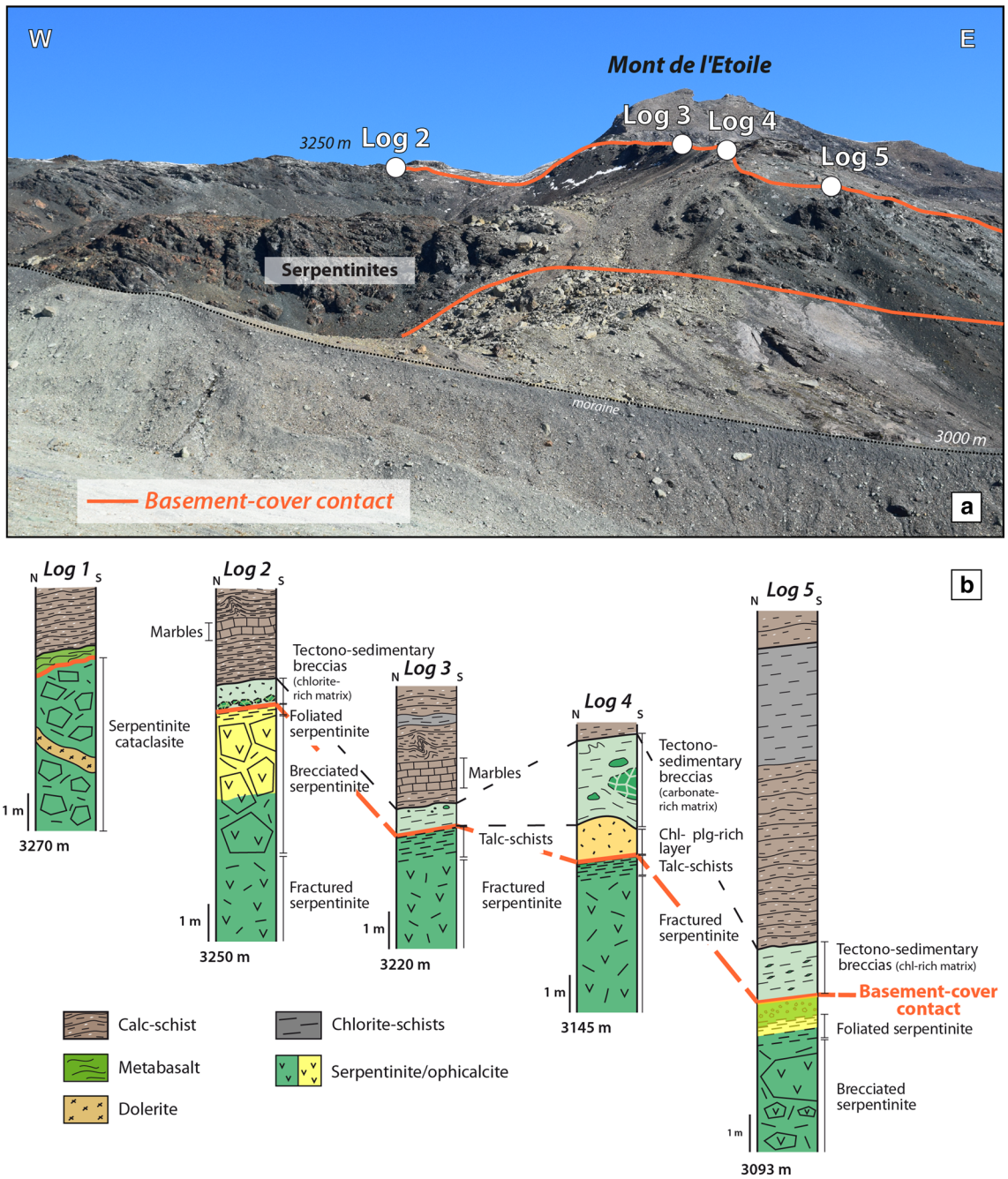

Fig. 7 **a** Panoramic view of the western flank of the Mont de l'Etoile displaying the contact between the serpentinized peridotite and the sedimentary cover. **b** Detailed lithological successions across the contact between the peridotite basement and the sedimentary cover. Log1 is located slightly to the left of the panorama. Its position is reported in the geological map (Fig. 2)

Black phyllites crop out in the Pointe de Darbonires area (Fig. 2) and are mainly composed of quartz, muscovite, and graphite. These rocks may result from the deposition of clay materials in a deep-sea environment characterized by anoxic conditions and therefore may represent Cretaceous black shales (Marthaler and Stampfli 1989).

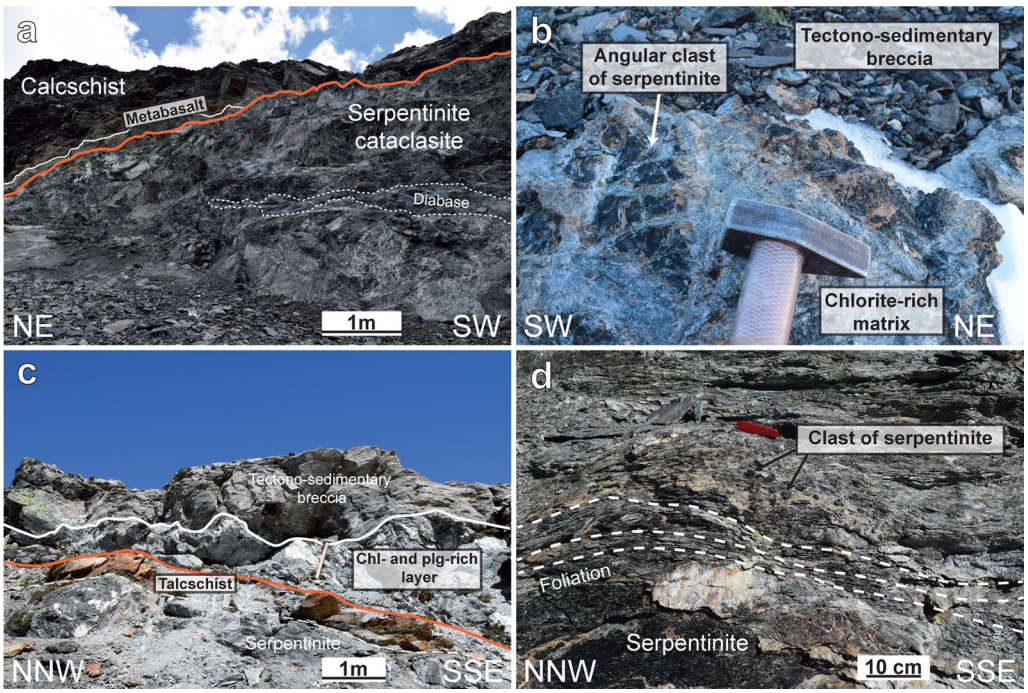

Fig. 8 Main field aspects of the basement-cover contact in the Mont de l'Etoile area. **a** Serpentinite cataclasite, intruded by a diabase at Log 1. Mantle rocks are overlain by a thin layer of metabasalt and calcschist. **b** Tectono-sedimentary breccia at Log 2 (overlying foliated serpentinite). The clasts of serpentinite are angular and still displaying the primary texture of mantle rocks. They are supported by a chlorite-rich matrix and show partial carbonatization. **c** Basement-cover sequence at Log 4. Serpentinite is transformed into a talcschist at the basement-cover interface. It is stratigraphically overlain by a chlorite- and plagioclase-rich layer of laterally variable thickness. The latter are sealed by a tectono-sedimentary breccia, including clasts of serpentinite within a carbonate-rich matrix. **d** Foliated and carbonatized serpentinite at Log 5

4.4 Geochemical results

4.4.1 Bulk rock chemistry

The Aiguilles Rouges gabbros display compositions rich in Al_2O_3 (15.0–19.3 wt%,) and CaO (6.7–12.4 wt%; Fig. 9), but low in alkalis. Low contents of Ni and Cr emphasize the absence of olivine and Cr-rich phases in the protolith. Gabbros have rather homogeneous bulk Mg# (molar $Mg/Mg+Fe_{tot}$, all Fe is Fe^{2+}) ranging from 0.69 to 0.73. Incompatible elements such as Ti, P and other HFSE (Fig. 9) are relatively low, despite the presence of ilmenite, apatite and zircon as accessory minerals. Chondrite-normalized REE patterns of the metagabbros (Fig. 10a) are typical of N-MORB (Ce_N/Yb_N: 0.42–0.74), with little fractionation between the LREE, and flat MREE and HREE (La_N/Sm_N: 0.30–0.49; Gd_N/Yb_N: 1.06–1.22). The gabbros all show a positive Eu anomaly (Eu/Eu*: 1.11–2.17) related to plagioclase accumulation. The total REE content is low (ΣREE = 13–21 ppm) and comparable to other samples from the Tsaté nappe (Manzotti et al. 2017). The mylonitic metagabbros are characterized by lower Mg# (0.56–0.69) and higher contents of TiO_2, P_2O_5 and other HFSE (Fig. 9), while Y correlates positively with Zr. This indicates that the mylonitized metagabbros are more differentiated than the undeformed gabbros. This is also evident by higher ΣREE values that are between ca. 34 and 56 ppm. The chondrite-normalized REE patterns also are typical of N-MORB compositions (Fig. 10b), with little fractionation of LREE compared to flat MREE and HREE (La_N/Sm_N: 0.49–0.72; Gd_N/Yb_N: 1.09–1.28). In contrast to the undeformed gabbro, the mylonitized metagabbros expose small positive or negative Eu anomalies (Eu/Eu*: 0.89–1.16), possibly related to variable amounts of interstitial liquid (Fig. 10b).

Basalts are rich in Al_2O_3 (14–21 wt%) and CaO (8–14.3 wt%), but low in alkalis. Bulk Mg# is between 0.51–0.65, and shows negative correlations with Ti, P, and other HFSE (Fig. 9). The trace element compositions are generally enriched compared to the metagabbro (Fig. 10a, b), illustrating the difference between gabbro cumulates and liquids. The ΣREE are ranging between 27–82 ppm. The chondrite-normalized REE patterns are characteristic of N-MORB basaltic rocks (Fig. 10a, b), with a weak depletion in LREE (La_N/Sm_N: 0.36–0.70) and flat M-HREE (Gd_N/Yb_N: 1–1.26). The Eu/Eu* values are slightly negative, ranging from 0.88–0.98.

The diabase dikes that intrude the Aiguilles Rouges Gabbro are rich in Al_2O_3 (ca. 13–17 wt% and CaO (ca. 8–14 wt%; Fig. 9), but depleted in alkali elements.

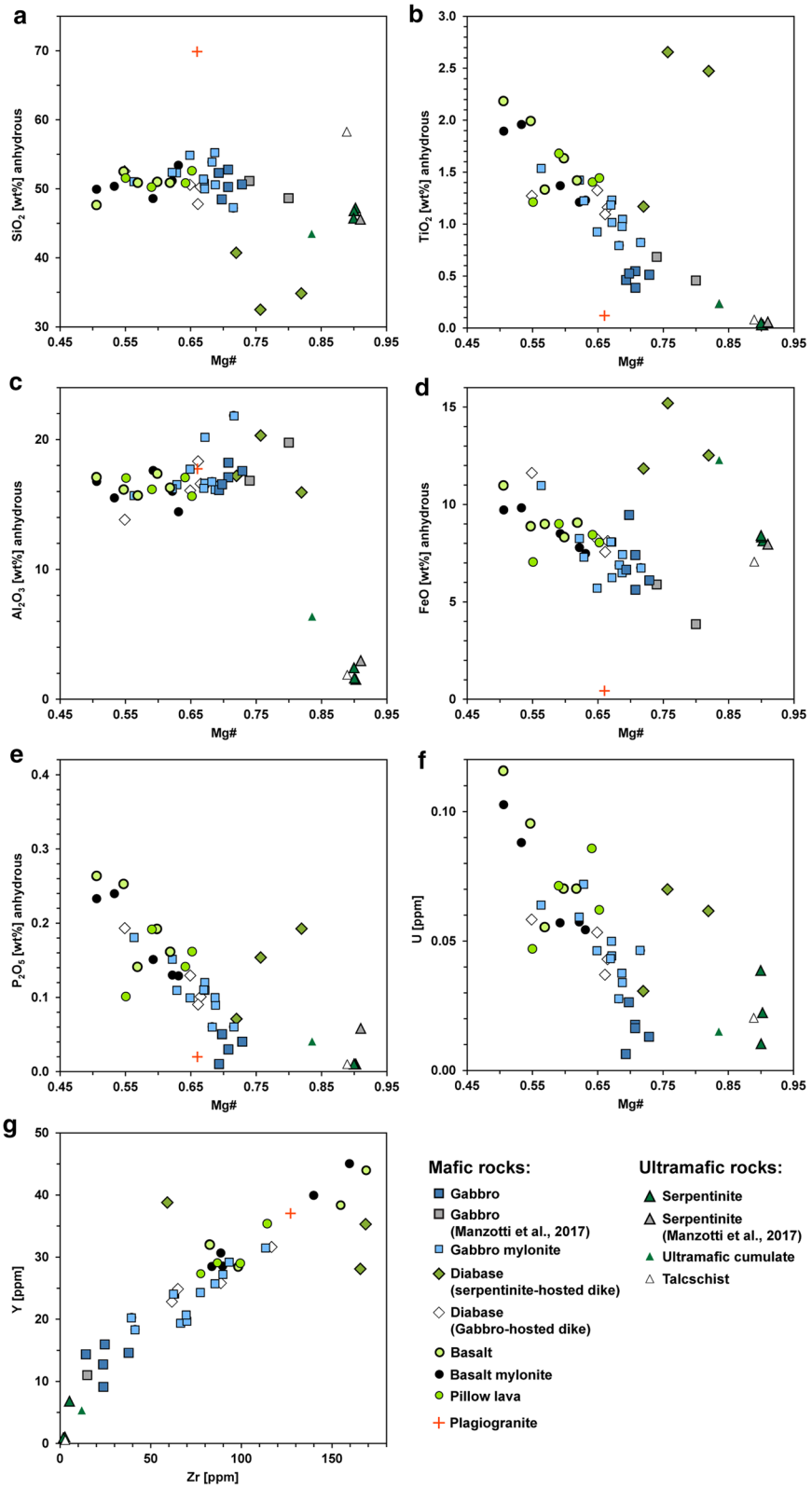

Fig. 9 Major and trace element variation diagrams of bulk rock compositions

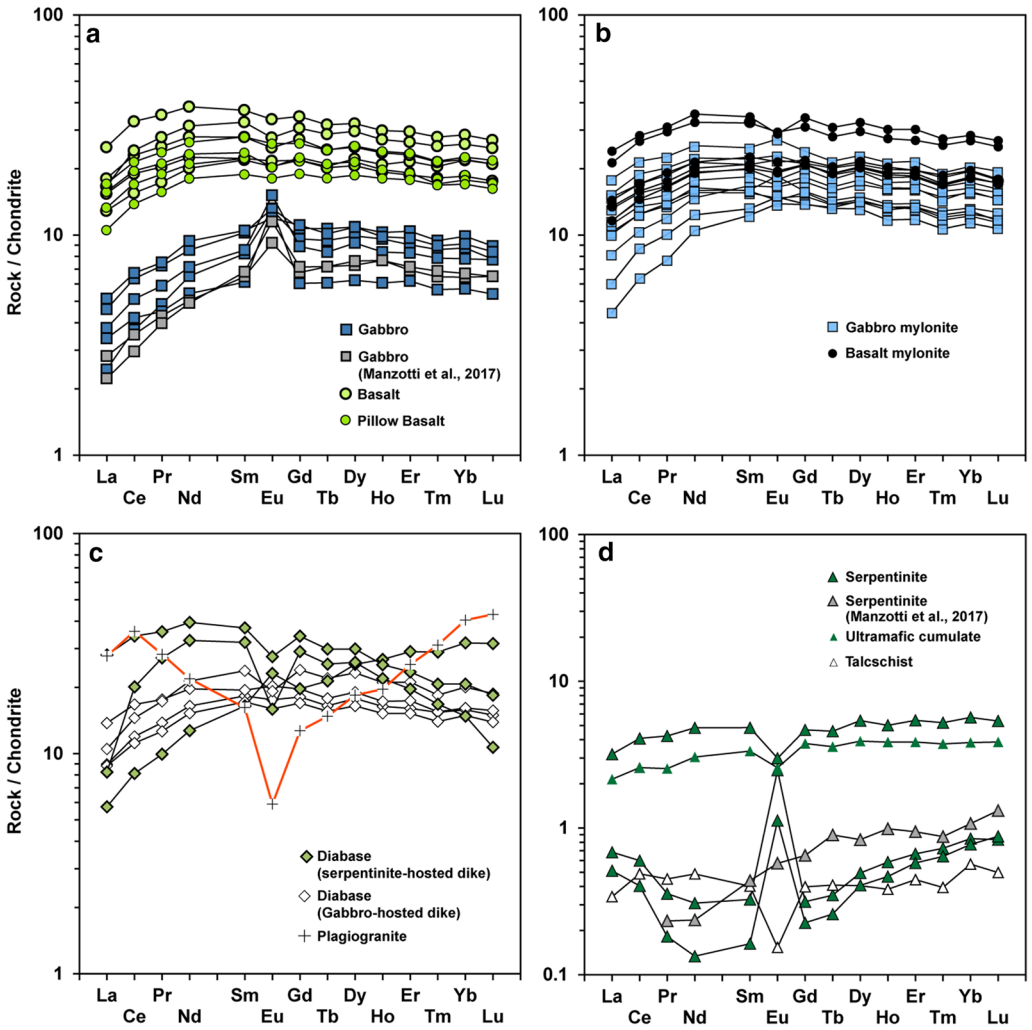

Fig. 10 Chondrite-normalized rare earth element patterns for ultramafic, mafic and felsic rocks from the Aiguilles Rouges ophiolites. Normalizing values are from McDonough and Sun (1995)

HFSE and U are negatively correlated with bulk Mg# (Fig. 9). Overall, the chemistry of the dikes is similar to the basalts. The trace element composition of the dikes is enriched in comparison to the metagabbro (Fig. 10c). The chondrite-normalized REE patterns are typical of N-MORB magmatic rocks (Fig. 9c), with little fractionation of LREE (La_N/Sm_N: 0.26–0.75) and flat M-HREE (Gd_N/Yb_N: 1.14–1.22). The ΣREE range from 35 to 45 ppm.

The diabase dikes that intrude the serpentinite are metasomatically altered with extremely low CaO content (< 2 wt%). The compositions of the dikes are also characterized by low SiO_2 and elevated MgO (Fig. 9), resulting in much higher Mg# for comparable trace element contents of the basalts. The samples display high TiO_2, FeO, P_2O_5 and Nb (Fig. 9), suggesting that these dikes are derived from a differentiated Fe–Ti–P–rich liquid. The chondrite-normalized REE patterns are hump-shaped (Fig. 10c), with LREE (La_N/Sm_N: 0.26–0.75) and M-HREE fractionation (Gd_N/Yb_N: 1.65 and 1.96, respectively) and characterized by a pronounced negative Eu anomaly (Eu/Eu*: 0.77–0.52).

The plagiogranites have the highest contents of SiO_2 and Na_2O (69.5 wt% and 9.9 wt%, respectively), but are extremely low in TiO_2, P_2O_5, FeO and MgO (Fig. 8), the bulk Mg# being 0.66. The trace element composition is enriched in HFSE (most notably in Th, U, Nb, Ta), compared to mafic and ultramafic rocks (Fig. 11). The chondrite-normalized REE pattern is "V" shaped (Fig. 10c), typical of plagiogranites (e.g. Rollinson 2015), with enriched LREE and HREE compared to MREE (La_N/Sm_N: 1.72; Gd_N/Yb_N: 0.31). The negative Eu anomaly (Eu/Eu*: 0.41) is related to significant plagioclase fractionation.

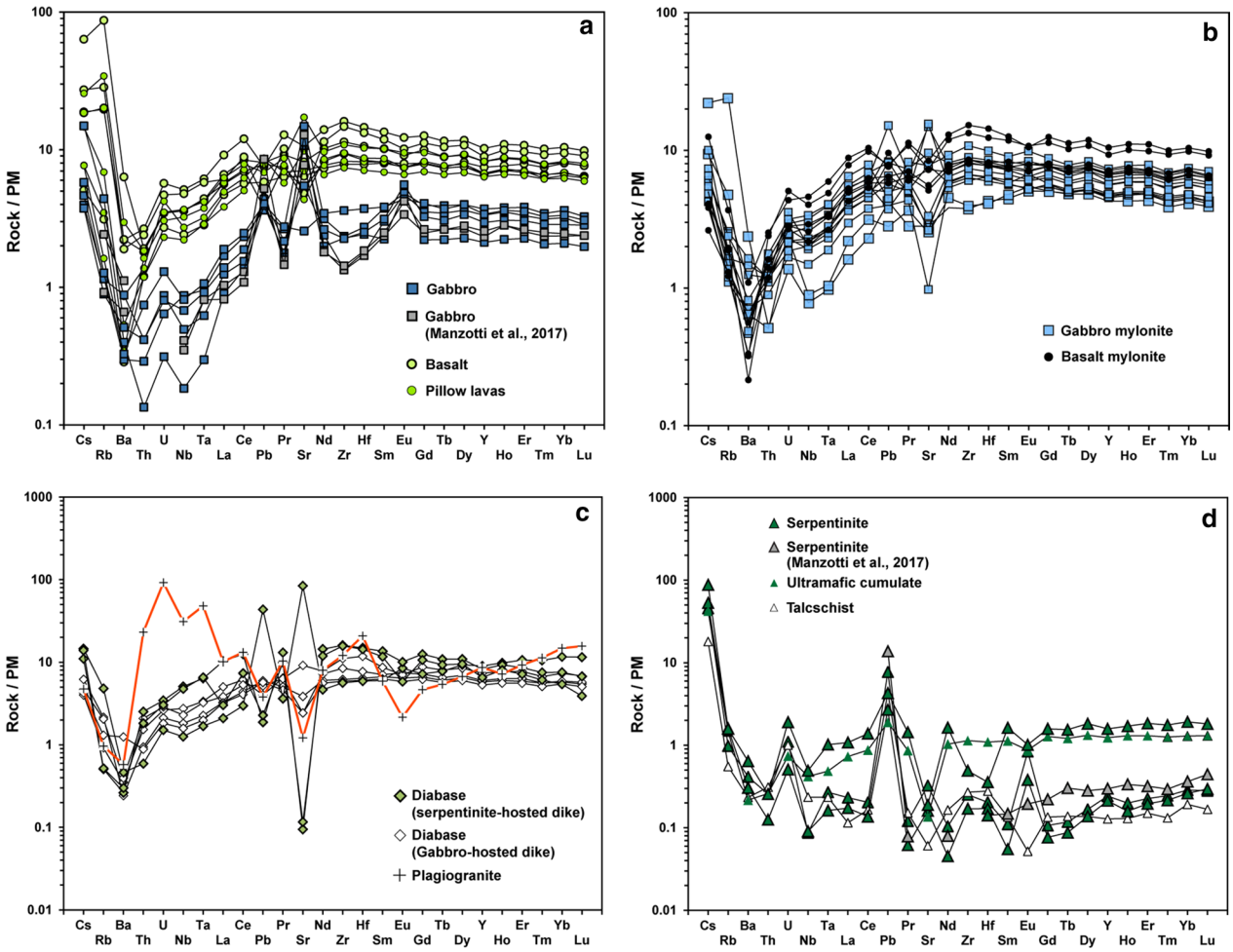

Fig. 11 Primitive mantle normalized trace element patterns for ultramafic, mafic and felsic rocks from the Aiguilles Rouges ophiolites. Normalizing values are from McDonough and Sun (1995)

Serpentinized peridotites are refractory (e.g. Bodinier and Godard 2014), based on low contents of TiO_2 (< 0.05 wt%) and Al_2O_3 (< 2.2 wt%). These rocks display homogenous bulk Mg# of ~ 0.90 and high concentrations of Ni (1929–2286 ppm) and Cr (2501–3592 ppm). The low CaO and Na_2O content are likely related to intense serpentinization. The flat REE patterns of samples LS6A and UM2 (Fig. 10d) are more enriched than lherzolites, and sample UM2 has significantly higher Al_2O_3, high Ni and low Cr content, a hallmark of olivine-rich troctolites. The "U" shaped pattern of the REE (Fig. 10d), in addition to MREE depletion (Gd_N/Yb_N: 0.29–0.37), compared to HREE (samples LS1 and S1) are characteristic of more depleted harzburgitic compositions (Bodinier and Godard 2014).

All rocks display significant enrichments in LIL elements (Fig. 11), which may reflect the effects of both seawater alteration and metamorphism. The serpentinites in addition are enriched in U (Fig. 11) and Pb, indicating interaction with seawater.

4.5 Texture, composition and U–Pb geochronology of zircon

An undeformed gabbro (sample 038MG, 46°03′24″ N 7°26′38″ E) and a hornblende-bearing felsic dikelet (sample DK1, 46°03′11″ N7°26′53″ E) intruding the Aiguilles Rouges Gabbro were selected for zircon dating. These two samples provided 11 and 20 crystals, respectively (Fig. 12).

4.5.1 Aiguilles Rouges Gabbro (038MG)

Zircon grains separated from the gabbro (038MG) are mainly transparent and free of inclusions, and range in size between 150 and 300 µm (Fig. 12a). Some crystals are entirely preserved and euhedral and display a morphology with pyramidal faces (e.g. grains 038MG-7 and

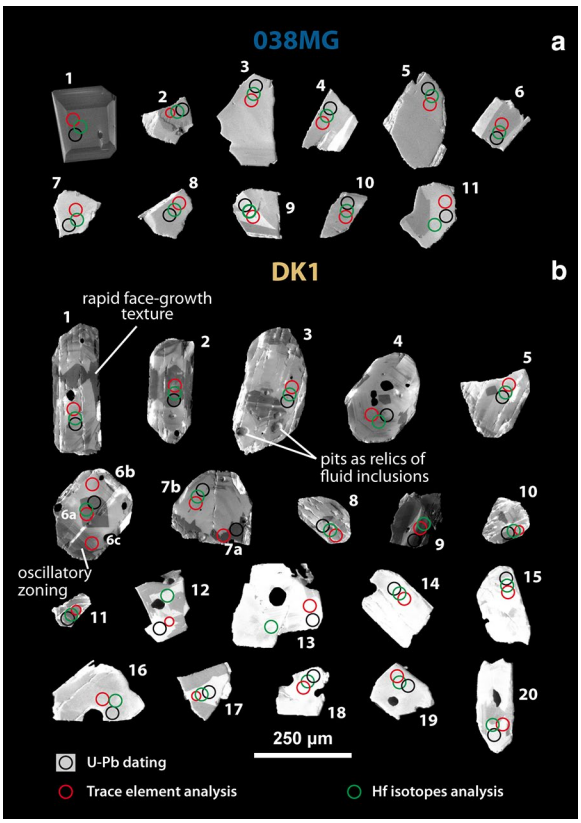

Fig. 12 Cathodoluminescence images of zircon crystals from samples 038GM (**a**) and DK1 (**b**). Black, red, and green circles indicate the location of LA-ICP-MS U–Pb dating, trace element analysis, and Hf isotope analysis, respectively. Labels refer to Additional file 1: Tables S4 and S5

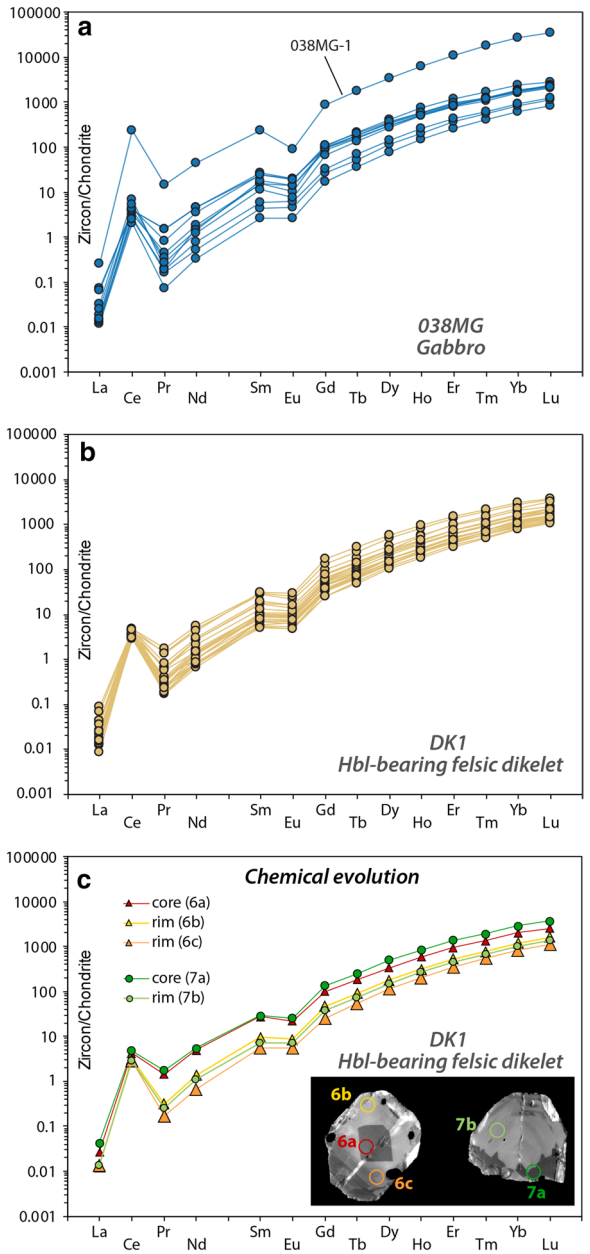

Fig. 13 Zircon trace element composition from samples 038MG (**a**) and DK1 (**b**). REE patterns are normalized to chondrite values of McDonough and Sun (1995). **c** Chemical evolution of zircon from core to rim for grains 6 and 7 in sample DK1

038MG-8; Fig. 12a). CL images reveal that the crystals are either not zoned, or alternatively, do not expose any complex growth zoning. The absence of complex zoning and the lack of inherited cores indicate a simple crystallization history.

The trace element chemistry of zircon is homogeneous, with similar normalized REE patterns. Only grain 038MG-1 displays a more enriched composition with respect to the other grains (Additional file 1: Table S3, and Fig. 13a). Minor chemical variations are related to the replacement of Zr^{4+} and Si^{4+} by Hf^{4+} and $Y+REE^{3+}$ in the crystal lattice. Zircon displays low U (7–54 ppm) and Th (3–31 ppm) contents, with the exception of grain 038MG-1 (321 ppm U and 271 ppm Th). The Th/U ratio ranges between 0.34 and 0.74 (Additional file 1: Table S4). The Ti content is also low and varies from 18 to 35 ppm, with a lowest value for grain 038MG-1 (8 ppm). Chondrite normalized REE patterns displays depletion in LREE and enrichment in HREE, a positive Ce (Ce/Ce* = 4.87–59.61) and negative Eu (Eu/Eu* = 0.16–0.34) anomaly (Fig. 13a). The negative Eu anomaly indicates that zircon crystallized after substantial fractionation of plagioclase. The zircon REE patterns and internal zoning are typical of igneous zircon (e.g. Hoskin and Schaltegger 2003). U–Pb analyses from zircon yielded $^{206}Pb/^{238}U$ dates ranging from 149.8 ± 6.4 Ma to 158.2 ± 3.6 Ma (2σ) (Additional file 1: Table S4). Eight concordant analyses (out of 11) yield a weighted mean age of 154.9 ± 2.6 Ma (95% c.l.; N = 8, MSWD = 1.8; Figs. 14a,b).

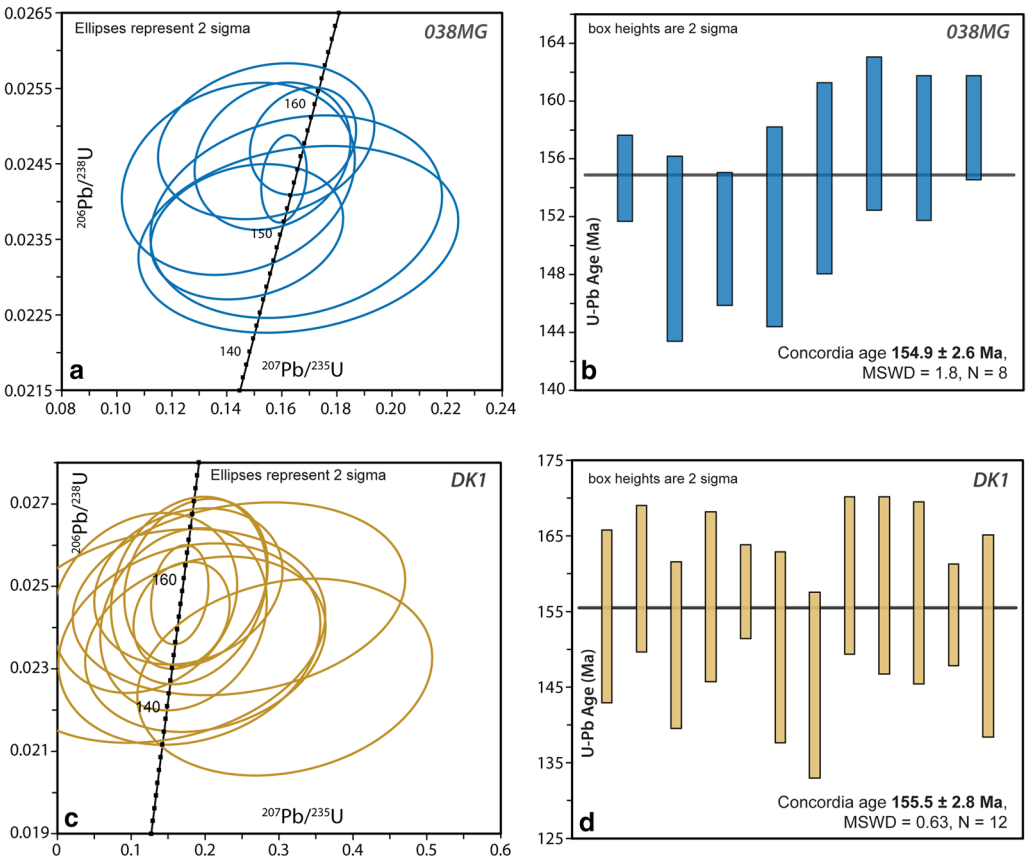

Fig. 14 Age results for the Aiguilles Rouges Gabbro. Concordia diagram for zircon analyses for samples 038MG (**a**) and DK1 (**c**). Weighted average ^{238}U-^{206}Pb age for samples 038MG (**b**) and DK1 (**d**)

4.5.2 Aiguilles Rouges hornblende-bearing felsic dikelet (DK1)

Zircon grains from the hornblende-bearing felsic dikelet (DK1) are transparent euhedral to subhedral (prismatic or squared), ranging in size from 150 to 450 µm (Fig. 12b). They display unsealed fractures characterised by invariant CL emissions, suggesting that these fractures were probably generated during crushing of the sample. Zircon crystals also show mineral or fluid inclusions up to 80 µm in size (pits and black spots on grains DK3-3 and DK3-4; Fig. 11b). Euhedral crystals are characterized by oscillatory zoning and rapid face-growth textures, typical for zircons from plagiogranites (e.g. Kaczmarek et al. 2008). No resorption features or inherited structures are observed.

Zircon crystals display low U (3–32 ppm) and Th (1–23 ppm) contents, and their Th/U ratio ranges from 0.31 to 0.71 (Additional file 1: Table S3). The Ti content is low (35–50 ppm). Measured Ba, Rb and Sr contents are low indicating that the analyses are largely unaffected by mineral inclusions or fractions. Chondrite-normalized REE patterns are similar, with HREE enrichment, a positive Ce (Ce/Ce*: 5.4–35.54) and negative Eu (Eu/Eu*: 0.26–0.35) anomaly (Fig. 13b). Microstructural observations suggest that zircon probably crystallized in-situ with hornblende, plagioclase and apatite, from a differentiated intercumulus melt saturated in Zr. This hypothesis is supported by the chemical evolution within zircon: chemical profiles on crystals DK1-6 and DK1-7 exhibit a progressive depletion in the REE content from core to rim, probably caused by the growth of zircon from a trapped liquid (Fig. 13c).

U–Pb analyses of zircon yield $^{206}Pb/^{238}U$ dates ranging from 139.3 ± 13.5 Ma to 169.4 ± 12.7 Ma (2σ) (Additional file 1: Table S4). Twelve concordant analyses (out of 20) define a weighted mean age of 155.5 ± 2.8 Ma (95% c.l.; N = 12, MSWD = 0.63; Fig. 14c, d).

4.6 In-situ Hf isotopes on zircon

In-situ Hf isotopic measurements are conducted on 8 zircon grains from sample 038MG and 12 zircons grains from sample DK-1. The measured $^{176}Hf/^{177}Hf$ ratios of the gabbro sample 038MG are fairly homogeneous and range between 0.283046 and 0.283118 (Additional file 1: Table S5) with an average of 0.283069 ± 0.000022. The initial $^{176}Hf/^{177}Hf_{CHUR}$ and $^{176}Lu/^{177}Hf_{CHUR}$ ratios were calculated using the ages determined by U–Pb dating by LA-ICP-MS (Additional file 1: Tables S2 and S4) and this results in a mean εHf(t) of $+12.95 \pm 0.42$ (2σ). For sample DK1, the measured $^{176}Hf/^{177}Hf$ ratios are comprised between 0.283044 and 0.283092 with an average of 0.283065 ± 0.000016, corresponding to a mean εHf (t) of $+13.01 \pm 0.56$ (2σ).

The εHf for both samples are identical within error indicating that zircon crystallized from melts produced by the same source. Such values are typical of a depleted mantle source (Nowell et al. 1998), in agreement with indications from the whole rock chemistry of the Aiguilles Rouges metagabbro. Hf isotopic compositions of zircon from accreted crust in the Piemonte-Liguria ocean will be further discussed in Sect. 6.3.

4.7 Sm–Nd isotopes of apatite

Sm–Nd isotope measurements were made on 11 apatite grains from sample 038MG and 10 apatite grains from sample DK-1. In both cases, the analyses returned fairly homogenous isotopic ratios. Measured $^{147}Sm/^{144}Nd$ for 038MG and DK-1 average to 0.155 ± 0.010 (2σ) and 0.140 ± 0.003 (2σ), respectively. The average measured $^{143}Nd/^{144}Nd$ are 0.513036 ± 0.000038 (2σ) for 038MG, and 0.513013 ± 0.000025 (2σ) for MG3. εNd calculated to the time of formation (155 Ma) are $+8.60 \pm 0.72$ (2σ) for 038MG and $+8.43 \pm 0.50$ (2σ) for MG3. As with the Lu–Hf isotope resultsabove, these values are consistent with magma derivation from a depleted mantle source (White and Klein 2014).

5 Discussion

5.1 Geological evidence for Jurassic inheritance

Our new field and geochemical data demonstrate that remnants of (ultra-) slow spreading oceanic crust are indeed present in the Aiguilles Rouges massif in the Val d'Hérens (Switzerland). Such remnants are also found in the Queyras and Civrari Western Alpine ophiolites and in the Northern Apennines (e.g. Lagabrielle et al. 2015; McCarthy and Müntener 2019; Tribuzio et al. 2016). The metamorphic Alpine overprint is weak, but Alpine deformation is locally intense and mainly localised in the metasediments and at the contact between the top of basalts and the base of the Aiguilles Rouges Gabbro. Despite the Alpine overprint, the primary structure of the oceanic lithosphere is still locally preserved, as manifest in the following:

- Primary magmatic texture and mineralogy (e.g. clinopyroxene, hornblende, zircon, apatite) are preserved in the kilometre-scale unstrained gabbro exposed in the Aiguilles Rouges Ophiolite. In addition, primary intrusive relationships between the main gabbro body and the intruding dikes (diabase, hornblende-bearing felsic dikes, and plagiogranite) have not been affected by the Alpine deformation.
- Relics of pillow lavas are preserved at the Mont des Ritses and above the Cabane des Aiguilles Rouges, implying the emplacement of basaltic magmas at the seafloor.
- The section between the Pointe des Darbonires and the Mont de l'Etoile (Fig. 2) exposes a kilometre-sized sheet of ultramafic basement closely associated with a sedimentary sequence that we consider to represent its own primary sedimentary cover. The primary ultramafic basement-cover contact is oriented in a normal position. This interpretation is supported by the presence of ultramafic clasts in the overlying carbonate sediments, but also the presence of talcschists and ophicalcite on top of the ultramafic basement. Both occurrences suggest the exposure of the ultramafic basement to the seafloor and consequently fluid-rock interactions. These features have been observed in exhumed mantle on the seafloor (e.g. Tricart and Lemoine 1983) and in other areas of the Alps and Appennines (Lemoine 1967; Lemoine et al. 1987; Lagabrielle and Cannat 1990; Lagabrielle 1994; Lagabrielle et al. 2015; Florineth and Froitzheim 1994; Treves and Harper 1994; Vitale Brovarone et al. 2011; Meresse et al., 2012; Epin et al. 2019). The occurrence of tectono-sedimentary breccias, containing clasts of ultramafic rocks suggests submarine tectonic activity prior to the deposition of calcschists. The lateral variations of the sedimentary record along the basement-cover contact suggest submarine topography, prior to sedimentation onto the exhumed mantle rocks. Such variations are unlikely to occur during Alpine reactivation. The metasedimentary sequence mainly comprises intervals of marbles and calcschists. By comparison with the lithostratigraphy in the Western Alps, this metasedimentary sequence may have been deposited during Upper Jurassic to Lower Cretaceous times (Lemoine et al. 1970; Lemoine 1971). Green bedded metacherts such as observed in comparable sedimentary sequences in

the Alps and Appennines and dated Oxfordian to Kimmeridgian in age (163.5–152.1 Ma; De Wever and Caby 1981; Schaaf et al. 1985; De Wever et al. 1987) are absent in the working area. This may be explained by the Late Jurassic age of the Aiguilles Rouges Ophiolite (~ 155 Ma, this study). However, this interpretation relies on the working hypothesis that Aiguilles Rouges and Mont de l'Etoile were close to each other during the oceanic evolution.

5.2 Magmatic evolution of the Aiguilles Rouges Gabbros

Gabbros of the Aiguilles Rouges are fairly homogenous and characterized by N-MORB compositions with bulk Mg# ranging from 0.69 to 0.73. They are slightly evolved with respect to primitive troctolites and olivine gabbros, typical of other gabbroic sequences in the Alps and Corsica (e.g. Kaczmarek et al. 2008; Sanfilippo and Tribuzio 2013). The gabbros show generally flat MREE and HREE between 5 and 10 times chondrite (Fig. 10), with little fractionation of LREE ($La_N/Sm_N = 0.3–0.75$), and positive Eu and Sr anomalies (Fig. 11). This indicates that the gabbros represent cumulates from which evolved melt has been fractionated. It is intriguing that the Aiguilles Rouges Gabbros do not present any magmatic layering. One possibility is that the gabbroic complex formed via repeated injection of similar MOR-type magmas, rather than a single crystallizing magmatic chamber. Single pulses may be discriminated by grain-size variations in the field (e.g. Fig. 4g). The rather homogeneous composition of the gabbro indicates a similar mantle source for the migrating magmas and similar differentiation processes at depth.

The plagiogranite and the hornblende-bearing felsic dikelets are subparallel and form a network of evolved melts enriched in incompatible elements and showing negative Eu and Sr anomalies, which imply fractionation of plagioclase (Fig. 10c). These liquids locally crystallized abundant apatite and zircon. U–Pb ages of both gabbro and plagiogranite are identical within error, indicating initial formation and late-stage migration and crystallization of evolved MOR-type melts, that are genetically related to the formation of oceanic crust at ~ 155 ± 2 Ma. Geochemical and in-situ Nd and Hf geochemical data on zircon and apatite indicate a N-MORB source and a Jurassic age for the Aiguilles Rouges Gabbro.

The metabasalts show N-MORB compositions with $Ce_N/Yb_N < 1$ and are very similar to the diabase dikes crosscutting the Aiguilles Rouges Gabbro. However, the diabase dikes are cut by mylonites on the eastern side of the Aiguilles Rouges. The intrusion of diabase dikes in gabbros and cataclastically deformed peridotites, and basaltic lava flows on the top of exhumed mantle indicate that magmatic activity is postdating the emplacement and cooling of the gabbro.

An intriguing aspect of the Aiguilles Rouges gabbros is the increasing abundance of Fe–Ti oxides and hornblende and generally higher REE and incompatible element contents (Fig. 10b) at its *base*, where high-temperature shear zones are preserved. While some of the (greenschist-facies) deformation at the base may be related to Alpine thrusting of the gabbros on top of the basalts, high temperature ductile deformation within Fe–Ti rich gabbros is typical for drilled gabbro sequences from (ultra-) slow spreading ridges and oceanic core complexes (e.g. Dick et al. 2000; Ildefonse et al. 2007). The finding of evolved gabbros at the base of a km-scale body is surprising. One hypothesis is that Alpine thrusting reactivated (Jurassic) fine-grained shear zones that previously acted as channels of evolved melts formed during crystallization of the Aiguilles Rouges Gabbro.

The diabase dikes intruding the Aiguilles Rouges Gabbro and serpentinized peridotites are a key element in the geological history of the Aiguilles Rouges area. The diabase dikes within the Aiguilles Rouges Gabbros are geochemically very similar to the basalts (Fig. 10c) and testify to continued MORB-type magmatic activity after solidification of the gabbros. It is tempting to relate the diabase dikes within the Aiguilles Rouges Gabbro with those cutting across cataclastic and serpentinized peridotites at Pointe des Darbonires and Col des Ignes. This would indicate that basaltic activity continues during exhumation of the Aiguilles Rouges Gabbros close to the surface and cataclastic deformation and exhumation of the peridotites on the seafloor.

In summary, field observations, major and trace element data of gabbros and basalts support the view that the Aiguilles Rouges area represents a piece of oceanic crust that is laterally segmented. The mantle-derived rocks are covered by sediments indicating that the seafloor in the northeastern part of the studied area has an ultramafic component. In contrast, the hornblende-bearing km-scale cumulate gabbros are typical of 'low temperature' oceanic crust of (ultra-) slow spreading ridges, perhaps representing the remnants of an 'oceanic core complex'. Residual liquid was extracted from the crystallizing gabbros along ductile shear zones and transported to shallower levels. Continued magmatic activity during exhumation is demonstrated by diabase dikes that cut peridotites and gabbros, and by lava flows and pillow basalts that locally covered the exhumed mantle rocks. In this view, the Aiguilles Rouges Gabbros were sheared off along hydrous oceanic shear zones and juxtaposed upon basaltic rock during Alpine convergence.

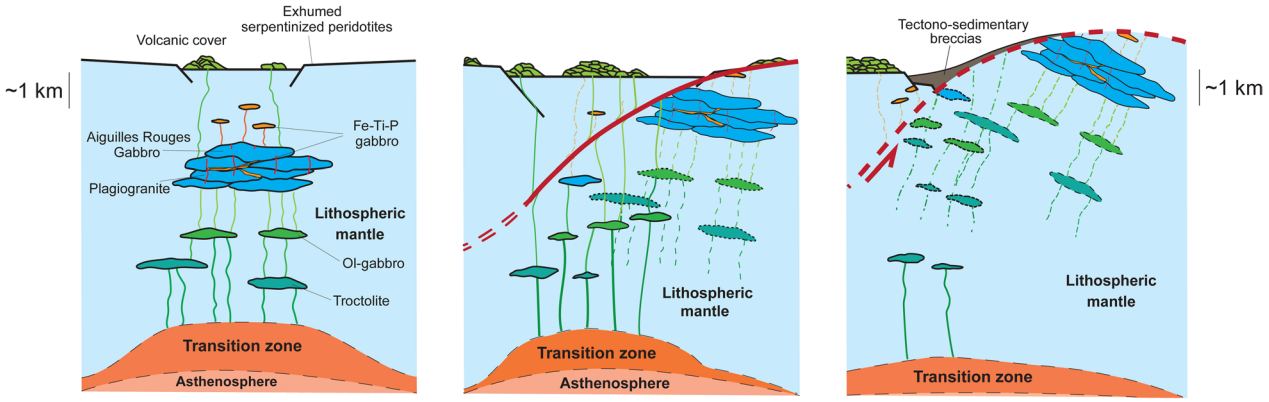

Fig. 15 Schematic model of the oceanic lithosphere from the Piemonte-Liguria basin based on observations from the Aiguilles Rouges Ophiolite. The model shows 3 snapshots on the interplay between deformation and magmatism. For further discussion, see text

5.3 Age and mantle sources of the Aiguilles Rouges Gabbro and regional importance

Zircons from oceanic gabbroic rocks of Alpine ophiolites have been dated previously [see summary in Manatschal and Müntener (2009), and some more recent work cited below], but with the exception of plagiogranites, none of the larger gabbroic masses provided an age substantially younger than 160 Ma. The ages from the Aiguilles Rouges Gabbro are amongst the youngest ages measured from Alpine ophiolites. They are clearly younger than the Liguria and Corsica ophiolites (e.g. Tribuzio et al. 2016; Li et al. 2015), and also younger than most mafic rocks from the Central and Western Alps (e.g. Bill et al. 1997; Rubatto et al. 1998; Schaltegger et al. 2002; Kaczmarek et al. 2008). Collectively, the new results combined with previously published data suggest that the magmatic activity recorded in remnants of the Piemonte Liguria ocean is relatively short lived, not exceeding 15 million years. However, this is likely to be a minimum, since it cannot be excluded that younger (or older) remnants of oceanic crust is either not yet dated or simply not preserved. Taking into account these caveats and the observation that Alpine ophiolites resemble ocean-continent transitions and / or (ultra-)slow-spreading ridges, the width of newly formed oceanic crust is probably not exceeding 300 km, taking an average plate separation rate of 2 cm/year as an upper limit.

Taking segmentation similar to the Southwest Indian Ridge into account (e.g. Cannat et al. 2019), magmatic activity might not be continuous but punctuated. Tectonic extension, core complex formation, and mantle exhumation might account for much of the extension between Europe and Adria.

Compiled Sr- and Nd isotope geochemical data on gabbros (e.g. Rampone and Hofmann 2012), εHf of zircon (Schaltegger et al. 2002; Li et al. 2013, 2015) and $\delta^{18}O$ of zircon from the Corsica and Chenaillet ophiolites (Li et al. 2013, 2015), support the view that the gabbros have sources compatible with a depleted MORB mantle source. The new εHf of zircon and the first εNd measurements of apatite for the Aiguilles Rouges Gabbro are compatible with this interpretation. Although the variability between Corsica ophiolites (+15.0 to +15.9; Li et al. 2015), the Platta ophiolite (+14.4 to 14.9; Schaltegger et al. 2002), the Chenaillet ophiolites (+13.0 to +13.5; Li et al. 2013) and the Aiguilles Rouges ophiolites (+12.5 to +13.6) is significant, it is currently not possible to speculate about regional or temporal variability. Our favoured interpretation as expressed here is based on the following 3 hypotheses that (i) elements from the whole oceanic lithosphere were sampled in the Alpine units; (ii) the isotopic age database is now sufficiently large to firmly establish the duration of the oceanic accretion; and (iii) the overall accretion rate and mechanisms were similar throughout the Tethyan domain. Future studies should exploit the internal variability of various ophiolites in greater detail to eventually establish temporal, regional or local trends.

5.4 Geodynamics of ultra-slow-spreading domains in the lost Piemonte-Liguria ocean: a model for the Aiguilles Rouge Gabbro

As discussed in Sect. 6.2, the observed field relationships suggest that the seafloor of the Piemonte-Liguria Ocean

is laterally segmented. In the following conceptual model, we account for plate separation to be accommodated by tectonic extension and magmatic accretion, similarly to present-day (ultra-) slow-spreading environments. The model is inspired by results from the Mid-Atlantic Ridge and Southwest Indian Ridge (e.g. Escartin et al. 2003; Cannat et al. 2006; Ildefonse et al. 2007; Tucholke et al. 2008; MacLeod et al. 2009).

The three-stage scenario developed in Fig. 15 is based upon: (a) the exposure of mantle rocks on the ocean floor; (b) the presence of discontinuous lavas overlying the basement rocks; (c) the emplacement of gabbroic complexes that might form 'oceanic core complexes (e.g. Ildefonse et al. 2007); (d) magma-starved seafloor spreading, accommodated by low angle detachment faulting and discontinuous crustal accretion; and (e) high-angle faults affecting the brittle uppermost part of the seafloor.

5.4.1 Phase 1: Emplacement of the gabbros

During phase 1 (ca. 155 Ma), batches of melt, produced by the partial melting of the MORB type asthenosphere, as indicated by εHf of zircon and εNd of apatite, are migrating and eventually reacting within the lithospheric mantle. Troctolites and olivine gabbros similar to those described in Corsica and the Northern Apennines are crystallizing at depth from mantle-derived melts. The residual melt will accumulate and form the Aiguilles Rouges Gabbro complex by fractionating pyroxene and plagioclase. The Aiguilles Rouges Gabbro was formed by rapid assembly and crystallization of several batches of melt from a similar mantle source. The crystallization and fractionation of repeated batches of melt may explain the formation of plagiogranite, and the evolution of evolved Fe–Ti gabbros and hornblende-bearing felsic dikelets crosscutting the main gabbros. It could also explain the grain-size variation observed within the internal part of the mafic intrusion. Evolved liquids were expelled at the top of the gabbroic complex, forming slightly evolved diabase and basalts. They are characterized by enriched compositions relative to the Aiguilles Rouges Gabbro and show weak negative Eu anomalies, indicating plagioclase fractionation.

5.4.2 Phase 2: Onset of detachment faulting and limited magmatic activity

During phase 2, the magmatic productivity is intermediate leading to alternating magma-rich and magma-starved episodes. A scenario similar to oceanic core complexes could arise during periods of limited magmatic activity, with the formation of a detachment fault exhuming the Aiguilles Rouges gabbroic body. The strain is progressively localized in the surrounding serpentinized peridotites, possibly causing some rigid rotation (see Ildefonse et al. 2007 and models of Lavier et al. 2000). The tectonic activity is accompanied by limited magmatic activity—the cold and brittle Aiguilles Rouges gabbroic body is crosscut by diabase of N-MORB composition (and possibly by evolved hornblende-rich felsic dikelets), that are residual from fractionating gabbros at depth. The diabase and hornblende-bearing dikelets crosscut the high-temperature foliation of the gabbro at high angle, forming a network, eventually feeding further basaltic activity at the surface.

5.4.3 Phase 3: Exhumation of the Aiguilles Rouges Gabbro along low-angle detachment faults

The Aiguilles Rouges Gabbro is partially exhumed, as well as the surrounding serpentinized peridotites, forming a typical dome shape. Faulting of the basement rocks and erosional processes produce tectono-sedimentary breccias (e.g. Lagabrielle et al. 2015) that are deposited and reworked onto the newly-formed oceanic floor. Mantle-derived melts are probably trapped and crystallized at depth within the footwall (Tucholke et al. 2008). No lavas are actively emitted at the surface (Tucholke et al. 2008; MacLeod et al. 2009).

6 Conclusions

The Tethyan Aiguilles Rouges ophiolites are built of kilometric slices of oceanic lithosphere, assembled during Alpine convergence. In the Val d'Arolla, two domains exposing inherited seafloor sequences were identified: the Aiguilles Rouges Ophiolite and the Mont de l'Etoile Ophiolite. They differ in terms of: (a) nature of basement rocks, (b) amount of mafic rocks, (c) basement-cover stratigraphy. A conceptual model of intermittent tectonism and magmatism can explain the lateral differences that were juxtaposed during Alpine convergence.

The proposed model bears some similarities with those described in other Tethyan ophiolites such as the Chenaillet, Queyras and Monviso ophiolites with the major difference that the Aiguilles Rouges complex exposes the remnants of a large gabbro body that has lost an evolved melt fraction. The preserved size is comparable to 'oceanic core complexes'.

Inferring a paleogeographic position to these ophiolites is a tricky exercise. In the Aiguilles Rouges area, the lack of continental crust material in the sedimentary record may be a good indicator of a more oceanward setting compared to that of an ocean-continent transition zone. This is supported by young crystallization age of ~ 155 Ma, but also by εHf of zircon and εNd of apatite

typical of a depleted N-MORB asthenosphere source. We propose that the Aiguilles Rouges ophiolites are segmented domains of the former Piemonte Liguria ocean, where magma-rich and magma-starved areas were formed close to each other, similar to areas mapped on the Southwest Indian Ridge.

Supplementary information

Supplementary information accompanies this paper at https://doi.org/10.1186/s00015-020-00380-4.

Additional file 1: Table S1. List of samples. **Table S2.** Bulk major and trace element chemistry. **Table S3.** Chemistry of zircon. **Table S4.** LA-ICPMS U–Pb dating of zircon. **Table S5.** Lu–Hf isotopic data of zircon. **Table S6.** Sm–Nd isotopic data of apatite. **Table S7.** RSCM thermometry on graphite.

Acknowledgements
We would like to thank Alexey Ulianov for precious help with Laser Ablation-ICP-MS analysis at UNIL and Massimo Chiaradia for help with Hf isotopes at the MC-ICPMS in Geneva. We thank Stefan Schmid, Mario Sartori and an anonymous reviewer for their comments to improve the paper. We especially acknowledge Yves Lagabrielle for pointing out some inconsistencies, and for sharing his knowledge on historical aspects of ophiolite research in the Alps, which greatly improved the presentation.

Authors' contributions
This work is part of TD's MSc thesis at the University of Lausanne. OM designed the project. TD, PM, RL, OM did field work and sampling. TD, PM, RL, CS processed and analysed samples. TD took the lead in writing the paper, all authors contributed to discussion and writing. All authors read and approved the final manuscript.

Funding
This research was funded by the Ambitione grant from the Swiss National Science foundation (Project PZ00P2_161202) and generous funding of the University of Lausanne.

Availability of data and materials
All the data produced and used in this paper are available as Additional file 1. Sample coordinates are in Additional file 1. Samples that were used to produce these data are stored at the University of Lausanne.

Competing interests
Not applicable.

Author details
[1] Institute of Earth Sciences, University of Lausanne, Géopolis, Quartier Mouline, 1015 Lausanne, Switzerland. [2] Géosciences Montpellier, University of Montpellier, CNRS, Montpellier, France. [3] Department of Geological Sciences, Stockholm University, 106 91, Stockholm, Sweden. [4] Geoscience, James Cook University, Townsville, QLD 4811, Australia.

Received: 18 May 2020 Accepted: 17 November 2020
Published online: 05 February 2021

References

Allimann, M. (1990). *La nappe du Mont Fort dans le Val d'Hérens: (zone pennique, Valais, Suisse)*. Unpublished MSc thesis, University of Lausanne, 109 p.

Angiboust, S., Glodny, J., Oncken, O., & Chopin, C. (2014). In search of transient subduction interfaces in the Dent Blanche-Sesia Tectonic System (W. Alps). *Lithos, 205,* 298–321. https://doi.org/10.1016/j.lithos.2014.07.001.

Anonymous. (1972). Penrose field conference on ophiolites. *Geotimes, 17,* 24–25.

Balestro, G., Festa, A., & Tartarotti, P. (2015). Tectonic significance of different block-in-matrix structures in exhumed convergent plate margins: examples from oceanic and continental HP rocks in Inner Western Alps (NW Italy). *International Geology Review, 57,* 581–605. https://doi.org/10.1080/00206814.2014.943307.

Ballèvre, M., & Lagabrielle, Y. (1994). Garnet in blueschist-facies marbles from the Queyras unit (Western Alps): its occurrence and its significance. *Schweizerische mineralogische und petrographische Mitteilungen, 74,* 203–212. https://doi.org/10.5169/seals-56342.

Bernoulli, D., & Jenkyns, H. C. (1974). Alpine, Mediterranean and Central Atlantic Mesozoic Facies in Relation to the Early Evolution of the Tethys. In R. H. Dott & R. H. Shaver (Eds.), *Modern and ancient geosynclinal sedimentation* (pp. 129–160). Tulsa: SEPM Society for Sedimentary Geology. https://doi.org/10.2110/pec.74.19.0129.

Beyssac, O., Goffé, B., Chopin, C., & Rouzaud, J. N. (2002). Raman spectra of carbonaceous material in metasediments: a new geothermometer. *Journal of Metamorphic Geology, 20,* 859–871. https://doi.org/10.1046/j.1525-1314.2002.00408.x.

Beyssac, O., Goffé, B., Petitet, J. P., Froigneux, E., Moreau, M., & Rouzaud, J. N. (2003). On the characterization of disordered and heterogeneous carbonaceous materials using Raman spectroscopy. *Spectrochimica Acta Part A: Molecular and Biomolecular Spectroscopy, 59,* 2267–2276. https://doi.org/10.1016/S1386-1425(03)00070-2.

Bickert, M., Lavier, L., & Cannat, M. (2020). How do detachment faults form at ultraslow mid-ocean ridges in a thick axial lithosphere? *Earth and Planetary Science Letters, 533,* 116408. https://doi.org/10.1016/j.epsl.2019.116048.

Bill, M., Bussy, F., Cosca, M., Masson, H., & Hunziker, J. C. (1997). High-precision U-Pb and 40Ar/39Ar dating of an Alpine ophiolite (Gets nappe, French Alps). *Eclogae Geologicae Helvetiae, 90,* 43–54. https://doi.org/10.5169/seals-168144.

Bill, M., O'Dogherty, L., Guex, J., Baumgartner, P. O., & Masson, H. (2001). Radiolarite ages in Alpine-Mediterranean ophiolites: Constraints on the oceanic spreading and the Tethys-Atlantic connection. *Geological Society of America Bulletin, 113,* 129–143. https://doi.org/10.1130/0016-7606(2001)113%3C0129:RAIAMO%3E2.0.CO;2.

Bodinier, J. L., & Godard, M. (2014). Orogenic, Ophioliitc and Abyssal Peridotites. In H. D. Holland & K. K. Turekian (Eds.), *Treatise on geochemistry: The mantle and core Pergamon* (Vol. 3, pp. 103–167). Netherlands: Elsevier. https://doi.org/10.1016/B978-0-08-095975-7.00204-7.

Boekhout, F., Spikings, R., Sempere, T., Chiaradia, M., Ulianov, A., & Schaltegger, U. (2012). Mesozoic arc magmatism along the southern Peruvian margin during Gondwana breakup and dispersal. *Lithos, 146,* 48–64. https://doi.org/10.1016/j.lithos.2012.04.015.

Boillot, G., Grimaud, S., Mauffret, A., Mougenot, D., Mergoil-Daniel, J., Kornprobst, J., & Torrent, G. (1980). Ocean-continent boundary off the Iberian margin: A serpentinite diapir west of the Galicia bank. *Earth and Planetary Science Letters, 48,* 23–34. https://doi.org/10.1016/0012-821X(80)90166-1.

Bonatti, E. (1971). Ancient continental mantle beneath oceanic ridges. *Journal of Geophysical Research, 76,* 3825–3831. https://doi.org/10.1029/JB076i017p03825.

Bonatti, E., & Honnorez, J. (1976). Sections of the earth's crust in the equatorial Atlantic. *Journal of the Geophysical Research, 81,* 4104–4117. https://doi.org/10.1029/JB081i023p04104.

Bouvier, A., Vervoort, J. D., & Patchett, P. J. (2008). The Lu–Hf and Sm-Nd isotopic composition of CHUR: Constraints from unequilibrated chondrites and implications for the bulk composition of terrestrial planets. *Earth and Planetary Science Letters, 273,* 48–57. https://doi.org/10.1016/j.epsl.2008.06.010.

Buck, R. W., Lavier, L. L., & Poliakov, A. N. B. (2005). Modes of faulting at mid-ocean ridges. *Nature, 434,* 719–723. https://doi.org/10.1038/nature03358.

Bugnon, C., Haarpaintner, T. (1979). *Etude géologique et minéralogique de la région d'Arolla, y compris le Grand et le Petit Mont Dolin*. Unpublished Diploma thesis, University of Lausanne.

Cann, J. R., Blackman, D. K., Smith, D. K., McAllister, E., Janssen, B., Mello, S., et al. (1997). Corrugated slip surfaces formed at ridge-transform intersections on the Mid-Atlantic Ridge. *Nature, 385,* 329–332. https://doi.org/10.1038/385329a0.

Cannat, M. (1993). Emplacement of mantle rocks in the seafloor at mid-ocean ridges. *Journal of the Geophysical Research, 98,* 4163–4172. https://doi.org/10.1029/92JB02221.

Cannat, M., Lagabrielle, Y., Bougault, H., Casey, J., de Coutures, N., Dmitriev, L., & Fouquet, Y. (1997). Ultramafic and gabbroic exposures at the Mid-Atlantic Ridge: Geological mapping in the 15°N region. *Tectonophysics, 279,* 193–213. https://doi.org/10.1016/S0040-1951(97)00113-3.

Cannat, M., Mevel, C., Maia, M., Deplus, C., Durand, C., Gente, P., et al. (1995). Thin crust, ultramafic exposures, and rugged faulting patterns at the Mid-Atlantic Ridge (22–24 N). *Geology, 23,* 49–52. https://doi.org/10.1130/0091-7613(1995)023%3C0049:TCUEAR%3E2.3.CO;2.

Cannat, M., Sauter, D., Lavier, L., Bickert, M., Momoh, E., & Leroy, S. (2019). On spreading modes and magmas supply at slow and ultraslow mid-ocean ridges. *Earth and Planetary Science Letters, 519,* 223–233. https://doi.org/10.1016/j.epsl.2019.05.012.

Cannat, M., Sauter, D., Mendel, V., Ruellan, E., Okino, K., Escartin, J., et al. (2006). Modes of seafloor generation at a melt-poor ultraslow-spreading ridge. *Geology, 34,* 605–608. https://doi.org/10.1130/G22486.1.

De Wever, P., Baumgartner, P. O., & Polino, R. (1987). Précision sur la datation de la base des Schistes Lustrés postophiolitiques dans les Alpes cottiennes. *Comptes rendus de l'Académie des Sciences Paris (II), 305,* 487–491.

De Wever, P., & Caby, R. (1981). Datation de la base des schistes lustrés post-ophiolitiques par des radiolaires (Oxfordien supérieur-Kimméridgien moyen) dans les Alpes Cottiennes (St-Véran, France). *Comptes rendus de l'Académie des Sciences Paris (II), 292,* 467–472.

Decandia, F. A., & Elter, P. (1969). Riflessioni sul problema delle ofioliti nell'Appennino Settentrionale (nota preliminare). *Atti della Società Toscana di Scienze Naturali, 75,* 1–9.

Desmurs, L., Müntener, O., & Manatschal, G. (2002). Onset of magmatic accretion within a magma-poor rifted margin: A case study from the Platta ocean-continent transition, eastern Switzerland. *Contributions to Mineralogy and Petrology, 144,* 365–382. https://doi.org/10.1007/s00410-002-0403-4.

Deville, E., Fudral, S., Lagabrielle, Y., Marthaler, M., & Sartori, M. (1992). From oceanic closure to continental collision: A synthesis of the "Schistes lustrés" metamorphic complex of the Western Alps. *GSA Bulletin, 104,* 127–139. https://doi.org/10.1130/0016-7606(1992)104%3C0127:FOCTCC%3E2.3.CO;2.

Dick, H. J. B., Lin, J., & Schouten, H. (2003). An ultraslow-spreading class of ocean ridge. *Nature, 426,* 405–412. https://doi.org/10.1038/nature02128.

Dick, H. J. B., Natland, J. H., Alt, J. C., Bach, W., Bideau, D., Gee, J. S., et al. (2000). A long in situ section of the lower ocean crust: Results of ODP Leg 176 drilling at the Southwest Indian Ridge. *Earth and Planetary Science Letters, 179,* 31–51. https://doi.org/10.1016/S0012-821X(00)00102-3.

Elter, G., Elter, P., Sturani, C., Weidmann, M. (1966). Sur la prolongation du domaine ligure de l'Apennin dans le Montserrat et les Alpes et sur l'origine de la Nappe de la Simme sl des Préalpes romandes et chablaisiennes. *Bulletin de la Société Vaudoise des Sciences Naturelles*, *65*(9).

Epin, M. E., Manatschal, G., Amman, M., Ribes, C., Clausse, A., Guffon, T., & Lescanne, M. (2019). Polyphase tectono-magmatic evolution during mantle exhumation in an ultra-distal, margin-poor rift domain: Example of the fossil Platta ophiolite, SE Switzerland. *International Journal of Earth Sciences, 18,* 2443–2467. https://doi.org/10.1007/s00531-019-01772-0.

Escartin, J., Mével, C., MacLeod, C. J., & McCaig, A. M. (2003). Constraints on deformation conditions and the origin of oceanic detachments: The Mid-Atlantic Ridge core complex at 15°45′N. *Geochemistry, Geophysics, Geosystems, 4,* 1–37. https://doi.org/10.1029/2002GC000472.

Ewing, T., Müntener, O., Leuthold, J., Ramìrez de Arellano, C., Baumgartner, L. P., & Schaltegger, U. (2019). The zircon Hf isotope archive of rapidly changing mantle sources in the south Patagonian retro-arc. *Geological Society of America Bulletin, 131,* 587–608. https://doi.org/10.1130/B31983.1.

Festa, A., Balestro, G., Dilek, Y., & Tartarotti, P. (2015). A Jurassic oceanic core complex in the high-pressure Monviso ophiolite (western Alps, NW Italy). *Lithosphere, 7,* 646–652. https://doi.org/10.1130/L458.1.

Fisher, C. M., McFarlane, C. R. M., Hanchar, J. M., Schmitz, M. D., Sylvester, P. J., Lam, R., & Longerich, H. P. (2011). Sm-Nd isotope systematics by laser ablation-multicollector-inductively coupled plasma mass spectrometry: Methods and potential natural and synthetic reference materials. *Chemical Geology, 284,* 1–20. https://doi.org/10.1016/j.chemgeo.2011.01.012.

Florineth, D., & Froitzheim, N. (1994). Transition from continental to oceanic basement in the Tasna nappe (Engadine window, Graubünden, Switzerland): evidence for Early Cretaceous opening of the Valais ocean. *Schweizerische mineralogische und petrographische Mitteilungen, 74,* 437–448. https://doi.org/10.5169/seals-56358.

Gillard, M., Autin, J., Manatschal, G., Sauter, D., Munschy, M., & Schaming, M. (2015). Tectonomagmatic evolution of the final stages of rifting along the deep conjugate Australian-Antarctic magma-poor rifted margins: Constraints from seismic observations. *Tectonics, 34,* 753–783. https://doi.org/10.1002/2015TC003850.

Girard, M. (2012). Originalkarte für den Gologischen Atlas der Schweiz, Blatt 1327 Evolène (Südteil). *Swisstopo*.

Glennie, K. W., Boeuf, M. G., Hughes-Clarke, M. H. W., Moody-Stuart, M., Pilaar, W. F., & Reinhardt, B. (1974). *Geology of the Oman Mountains* (p. 31). Geologisch Mijnbouwkundig Genootschap: Verhandelingen Koninklijk.

Groppo, C., Rinaudo, C., Cairo, S., Gastaldi, D., & Compagnoni, R. (2006). Micro-Raman spectroscopy for a quick and reliable identification of serpentine minerals from ultramafics. *European Journal of Mineralogy, 18,* 319–329. https://doi.org/10.1127/0935-1221/2006/0018-0319.

Hagen, T. (1948). *Geologie des Mont Dolin und des Nordrandes der Dent Blanche-Decke zwischen Mont Blanc de Cheilon und Ferpècle (Wallis)* (p. 64). Bern: Kuemmerly und Frey.

Hammerli, J., Kemp, A. I. S., & Spandler, C. (2014). Neodymium isotope equilibration during crustal metamorphism revealed by in situ microanalysis of REE-rich accessory minerals. *Earth and Planetary Science Letters, 392,* 133–142. https://doi.org/10.1016/j.epsl.2014.02.018.

Handy, M. R., Schmid, S. M., Bousquet, R., Kissling, E., & Bernoulli, D. (2010). Reconciling plate-tectonic reconstructions of Alpine Tethys with the geological-geophysical record of spreading and subduction in the Alps. *Earth-Science Reviews, 102,* 121–158. https://doi.org/10.1016/j.earscirev.2010.06.002.

Hopson, C. A., Coleman, R. G., Gregory, R. T., Pallister, J. S., & Bailey, E. H. (1981). Geologic Section Through the Samail Ophiolite and Associated Rocks Along a Muscat-Ibra Transect, Southeastern Oman Mountains. *Journal of Geophysical Research, 86,* 2527–2544. https://doi.org/10.1029/JB086iB04p02527.

Hoskin, P. W. O., & Schaltegger, U. (2003). The Composition of Zircon and Igneous and Metamorphic Petrogenesis. *Reviews in Mineralogy and Geochemistry, 53,* 27–62. https://doi.org/10.2113/0530027.

Ildefonse, B., Blackman, D. K., John, B. E., Ohara, Y., Miller, D. J., & MacLeod, C. J. (2007). Integrated Ocean Drilling Program Expeditions 304/305 Science Party. Oceanic core complexes and crustal accretion at slow-spreading ridges. *Geology, 35,* 623–626. https://doi.org/10.1130/G23531A.1.

Jackson, S. E. (2008). Calibration strategies for elemental analysis by LA-ICP-MS. In P. Sylvester (Ed.), *Laser ablation-ICP-MS in the earth sciences: Current practices and outstanding issues, Short course series* (Vol. 40, pp. 169–188). Mineralogical Association of Canada: Québec.

Kaczmarek, M.-A., Müntener, O., & Rubatto, D. (2008). Trace element chemistry und U-Pb dating of zircons from oceanic gabbros and their relationship with whole rock composition. *Contributions to Mineralogy and Petrology, 155,* 295–312. https://doi.org/10.1007/s00410-007-0243-3.

Karson, J. A. (1990). Seafloor spreading on the Mid-Atlantic Ridge: implications for the structure of ophiolites and oceanic lithosphere produced in slow-spreading environments. In J. Malpas, E. M. Moores, A. Panyiotou, & C. Xenophontos (Eds.), *Ophiolites: Oceanic crustal analogues* (pp. 547–555). Nicosia: Geological Survey Department.

Karson JA, Lawrence RM (1997) Tectonic setting of serpentinite exposure on the western median valley wall of the MARK area in the vicinity of site 920. In: Karson JA, Cannat M, Miller DJ, Elthon D (Eds.). *Proceedings of the Ocean Drilling Programs, Scientific Results*, 153, pp. 5–21.

Kunz, P. (1988). Ophiolites penniques et sediments associés dans la region d'Arolla (val d'Hérens, Valais, Suisse). *Eclogae Geologicae Helvetiae, 81,* 115–124. https://doi.org/10.5169/seals-166172.

Lagabrielle, Y. (1994). Ophiolites of the southwestern Alps and the structure of the Tethyan oceanic lithosphere. *Ofioliti, 19,* 413–434.

Lagabrielle, Y., & Auzende, J. M. (1982). Active in situ disaggregation of oceanic crust and mantle on Gorringe Bank: analogy with ophiolitic massives. *Nature, 297,* 490–493. https://doi.org/10.1038/297490a0.

Lagabrielle, Y., & Cannat, M. (1990). Alpine jurassic ophiolites resemble the modern central atlantic basement. *Geology, 18,* 319–322. https://doi.org/10.1130/0091-7613(1990)018%3C0319:AJORTM%3E2.3.CO;2.

Lagabrielle, Y., Lemoine, M., & Tricart, P. (1985). Paléotectonique océanique et deformations alpines dans le massif ophiolitique du Pelvas d'Abriès (Alpes Occidentales-Queyras-France). *Bulletin de la Societe géologique de France, 4,* 473–480. https://doi.org/10.2113/gssgfbull.I.4.473.

Lagabrielle, Y., Vitale Brovarone, A., & Ildefonse, B. (2015). Fossil oceanic core complexes recognized in the blueschist metaophiolites of Western Alps and Corsica. *Earth-Science Reviews, 141,* 1–26. https://doi.org/10.1016/j.earscirev.2014.11.004.

Lavier, L. L., Buck, W. R., & Poliakov, A. N. (2000). Self-consistent rolling-hinge model for the evolution of large-offset low-angle normal faults. *Geology, 27,* 1127–1130. https://doi.org/10.1016/j.epsl.2019.05.012.

Lemoine, M. (1967). Brèches sédimentaires marines à la frontière entre les domaines briançonnais et piémontais dans les Alpes occidentales. *Geologische Rundschau, 56,* 320–335. https://doi.org/10.1007/BF01848723.

Lemoine, M. (1971). Données nouvelles sur la série du Gondran près Briançon (Alpes Cottiennes). Réflexions sur les problèmes stratigraphique et paléogéographique de la zone piémontaise. *Géologie Alpine, 47,* 181–201.

Lemoine, M. (1985). Structuration jurassique des Alpes occidentales et palinspastique de la Tethys ligure. *Bulletin de la Société Géologique de France, I,* 127–137. https://doi.org/10.2113/gssgfbull.I.1.127.

Lemoine, M., Boillot, G., & Tricart, P. (1987). Ultramafic and gabbroic ocean floor of the Ligurian Tethys (Alps, Corsica, Apennines): in search of a genetic model. *Geology, 15,* 622–625. https://doi.org/10.1130/0091-7613(1987)15%3C622:UAGOFO%3E2.0.CO;2.

Lemoine, M., Steen, D., & Vuagnat, M. (1970). Sur le problème stratigraphique des ophiolites piémontaises et des roches sédimentaires associées: observations dans le massif de Chabrière en Haute-Ubaye (Basses-Alpes, France). *Compte Rendu des Séances de la Société de Physique et d'Histoire Naturelle de Genève, 5,* 44–59.

Li, X. H., Faure, M., Lin, W., & Manatschal, G. (2013). New isotopic constraints on age and magma genesis of an embryonic oceanic crust: The Chenaillet Ophiolite in the Western Alps. *Lithos, 160–161,* 283–291. https://doi.org/10.1016/j.lithos.2012.12.016.

Li, X. H., Faure, M., Rossi, P., Lin, W., & Lahondère, D. (2015). Age of Alpine Corsica ophiolites revisited: Insights from in situ zircon U-Pb age and O-Hf isotopes. *Lithos, 220–223,* 179–190. https://doi.org/10.1016/j.lithos.2015.02.006.

Lombardo, B., & Pognante, U. (1982). Tectonic implications in the evolution of the western Alps ophiolite metagabbro. *Ofioliti, 7,* 371–394.

Lombardo, B., Rubatto, D., & Castelli, D. (2002). Ion microprobe U-Pb dating of zircon from a Monviso metaplagiogranite: Implications for the evolution of the Piedmont-Liguria Tethys in the Western Alps. *Ofioliti, 27,* 109–117.

Longerich, H. P., Jackson, S. E., & Günther, D. (1996). Inter-laboratory note. Laser ablation inductively coupled plasma mass spectrometric transient signal data acquisition and analyte concentration calculation. *Journal of Analytical Atomic Spectrometry, 11,* 899–904. https://doi.org/10.1039/JA9961100899.

Ludwig, K.R. (2012). User's manual for isoplot 3.75. A geochronological toolkit for microsoft excel. *Berkeley Geochronology Center Special Publication*, *5*.

MacLeod, C. J., Escartin, J., Banerji, D., Banks, G. J., Gleeson, M., Irving, D. H. B., et al. (2002). Direct geological evidence for oceanic detachment faulting: The Mid-Atlantic Ridge, 15°45'N. *Geology, 30,* 879–882. https://doi.org/10.1130/0091-7613(2002)030%3C0879:DGEFOD%3E2.0.CO;2.

MacLeod, C. J., Searle, R. C., Murton, B. J., Casey, J. F., Mallows, C., Unsworth, S. C., et al. (2009). Life cycle of oceanic core complexes. *Earth and Planetary Science Letters, 287,* 333–344. https://doi.org/10.1016/j.epsl.2009.08.016.

Manatschal, G., & Müntener, O. (2009). A type sequence across an ancient magma-poor ocean-continent transition: the example of the western Alpine Tethys ophiolites. *Tectonophysics, 473,* 4–19. https://doi.org/10.1016/j.tecto.2008.07.021.

Manatschal, G., & Nievergelt, P. (1997). A continent-ocean transition recorded in the Err and Platta nappes (Eastern Switzerland). *Eclogae Geologicae Helvetiae, 90,* 3–27. https://doi.org/10.5169/seals-168142.

Manatschal, G., Sauter, D., Karpoff, A. M., Masini, E., Mohn, G., & Lagabrielle, Y. (2011). The Chenaillet ophiolite in the French/Italian Alps: An ancient analogue for an oceanic core complex? *Lithos, 124,* 169–184. https://doi.org/10.1016/j.lithos.2010.10.017.

Manzotti, P., Ballèvre, M., & Dal Piaz, G. V. (2017). Continental gabbros in the Dent Blanche Tectonic System (Western Alps): From the pre-Alpine crustal structure of the Adriatic paleo-margin to the geometry of an alleged subduction interface. *Journal of the Geological Society, 174,* 541–556. https://doi.org/10.1144/jgs2016-071.

Manzotti, P., Ballèvre, M., Zucali, M., Robyr, M., & Engi, M. (2014). The tectono-metamorphic evolution of the Sesia-Dent Blanche nappes (internal Western Alps): Review and synthesis. *Swiss Journal of Geosciences, 107,* 309–336. https://doi.org/10.1007/s00015-014-0172-x.

Marthaler, M. (1984). Géologie des unités penniques entre le val d'Anniviers et le val de Tourtemagne (Valais, Suisse). *Eclogae Geologicae Helvetiae, 77,* 395–448. https://doi.org/10.5169/seals-165516.

Marthaler, M. (2010). Originalkarte für den Gologischen Atlas der Schweiz, Blatt 1326 Rosablanche (östlicher Teil). *Swisstopo.*

Marthaler, M., & Stampfli, G. M. (1989). Les Schistes lustrés à ophiolites de la nappe du Tsaté: un ancien prisme d'accrétion de la marge active apulienne? *Schweizerische mineralogische und petrographische Mitteilungen, 69,* 211–216. https://doi.org/10.5169/seals-52789.

McCarthy, A., & Müntener, O. (2019). Evidence for ancient fractional melting, cryptic refertilization and rapid exhumation of Tethyan mantle (Civrari Ophiolite, NW Italy). *Contributions to Mineralogy and Petrology, 174,* 69. https://doi.org/10.1007/s00410-019-1603-5.

McDonough, W. F., & Sun, S. S. (1995). The composition of the Earth. *Chemical Geology, 120,* 223–253. https://doi.org/10.1016/0009-2541(94)00140-4.

Meresse, F., Lagabrielle, Y., Malavieille, J., & Ildefonse, B. (2012). A fossil Ocean-Continent Transition of the Mesozoic Tethys preserved in the Schistes Lustrés nappe of northern Corsica. *Tectonophysics, 579,* 4–16. https://doi.org/10.1016/j.tecto.2012.06.013.

Miyashiro, A., Shido, F., & Ewing, M. (1969). Composition and Origin of Serpentinites from the Mid-Atlantic Ridge near 24°and 30° North Latitude. *Contributions to Mineralogy and Petrology, 23,* 117–127. https://doi.org/10.1007/BF00375173.

Molli, G. (1996). Pre-orogenic tectonic framework of the northern Apennine ophiolites. *Eclogae Geologicae Helvetiae, 89,* 163–180. https://doi.org/10.5169/seals-167898.

Molli, G. (2008). Northern Apennine-Corsica orogenic system: an updated overview. In S. Siegesmund, B. Fugenschuh, & N. Froitzheim (Eds.), *Tectonic Aspects of the Alpine-Dinaride-Carpathian System, Special Publications* (Vol. 298, pp. 413–442). London: Geological Society. https://doi.org/10.1144/SP298.19.

Moores, E. M., & Vine, F. J. (1971). The Troodos Massif, Cyprus, and other ophiolites as oceanic crust: Evaluation and implications. *Philosophical Transactions of the Royal Society Series A, Mathematical and Physical Sciences, 268,* 443–466. https://doi.org/10.1098/rsta.1971.0006.

Müntener, O., & Hermann, J. (1996). The Val Malenco lower crust—upper mantle complex and its field relations (Italian Alps). *Schweizerische mineralogische und petrographische Mitteilungen, 76,* 475–500. https://doi.org/10.5169/seals-57711.

Nicolas, A., & Boudier, F. (1995). Mapping oceanic ridge segments in Oman ophiolite. *Journal of Geophysical Research, 100,* 6170–6197. https://doi.org/10.1029/94JB01188.

Nicolas, A., Boudier, F., & Meshi, A. (1999). Slow spreading accretion and mantle denudation in the Mirdita ophiolite (Albania). *Journal of Geophysical Research, 100,* 6170–6197. https://doi.org/10.1029/94JB01188.

Nowell, G. M., Kempton, P. D., Noble, S. R., Fitton, J. G., Saunders, A. D., Mahoney, J. J., & Taylor, R. N. (1998). High precision Hf isotope measurements of MORB and OIB by thermal ionisation mass spectrometry: Insights into the depleted mantle. *Chemical Geology, 149,* 211–233. https://doi.org/10.1016/S0009-2541(98)00036-9.

Pearce, N. J. G., Perkins, W. T., Westgate, J. A., Gorton, M. P., Jackson, S. E., Neal, C. R., & Chenery, S. P. (1997). A compilation of new and published major and trace element data for NIS SRM 610 and NIST SRM 612 Glass Reference Materials. *Geostandards Newsletter, 21,* 115–144. https://doi.org/10.1111/j.1751-908X.1997.tb00538.x.

Rampone, E., & Hofmann, A. W. (2012). A global overview of isotopic heterogeneities in the oceanic mantle. *Lithos, 148,* 247–261. https://doi.org/10.1016/j.lithos.2012.06.018.

Renna, M. R., Tribuzio, R., Sanfilippo, A., & Tiepolo, M. (2017). Zircon U-Pb geochronology of lower crust and quartzo-feldspathic clastic sediments

from the Balagne ophiolite (Corsica). *Swiss Journal of Geosciences, 110,* 479–501. https://doi.org/10.1007/s00015-016-0239-y.
Reston, T. J., & McDermott, K. G. (2011). Successive detachment faults and mantle unroofing at magma-poor rifted margins. *Geology, 39,* 1071–1074. https://doi.org/10.1130/G32428.1.
Rollinson, H. (2015). Slab and sediment melting during subduction initiation: granitoid dykes from the mantle section of the Oman ophiolite. *Contributions to Mineralogy and Petrology, 170,* 32. https://doi.org/10.1007/s00410-015-1177-9.
Rubatto, D., Gebauer, D., & Fanning, M. (1998). Jurassic formation and Eocene subduction of the Zermatt-Saas-Fee ophiolites: Implications for the geodynamic evolution of the Central and Western Alps. *Contributions to Mineralogy and Petrology, 132,* 269–287. https://doi.org/10.1007/s004100050421.
Sanfilippo, A., & Tribuzio, R. (2013). Building of the deepest crust at a fossil slow-spreading centre (Pineto gabbroic sequence, Alpine Jurassic ophiolites). *Contributions to Mineralogy and Petrology, 165,* 705–721. https://doi.org/10.1007/s00410-012-0831-8.
Sartori, M. (1987). Structure de la zone du Combin entre les Diablons et Zermatt (Valais). *Eclogae Geologicae Helvetiae, 80,* 789–814. https://doi.org/10.5169/seals-166026.
Schaaf, A., Polino, R., & Lagabrielle, Y. (1985). Nouvelle découverte de radiolaires d'âge Oxfordien supérieur-Kimméridgien inférieur, à la base d'une série supraophiolitique des schistes lustrés piémontais (Massif de Traversiera, Haut Val Maïra, Italie). *Comptes rendus de l'Académie des Sciences Paris (II), 301,* 1079–1084.
Schaltegger, U., Desmurs, L., Manatschal, G., Müntener, O., Meier, M., Frank, M., & Bernoulli, D. (2002). The transition from rifting to sea-floor spreading within a magma-poor rifted margin: Field and isotopic constraints. *Terra Nova, 14,* 156–162. https://doi.org/10.1046/j.1365-3121.2002.00406.x.
Schmid, S. M., Fügenschuh, B., Kissling, E., & Schuster, R. (2004). Tectonic map and overall architecture of the Alpine orogen. *Eclogae Geologicae Helvetiae, 97,* 93–117. https://doi.org/10.1007/s00015-004-1113-x.
Shemenda, A. I., & Grocholski, A. L. (1994). Physical modeling of slow seafloor spreading. *Journal of Geophysical Research, 99,* 9137–9153. https://doi.org/10.1029/93JB02995.
Sláma, J., Kostler, J., Condon, D. J., Crowley, J. L., Gerder, A., Hanchar, J. M., et al. (2008). Plešovice zircon—a new natural reference material for U-Pb and Hf isotopic microanalysis. *Chemical Geology, 249,* 1–35. https://doi.org/10.1016/j.chemgeo.2007.11.005.
Smith, D. K., Cann, J. R., & Escartin, J. (2006). Widespread active detachment faulting and core complex formation near 13° N on the Mid-Atlantic Ridge. *Nature, 442,* 440–443. https://doi.org/10.1038/nature04950.
Spandler, C., Hammerli, J., Sha, P., Hilbert-Wolf, H., Hu, Y., Roberts, E. M., & Schmitz, M. (2016). MKED1: A new titanite standard for in situ analysis of Sm-Nd isotopes and U-Pb geochronology. *Chemical Geology, 425,* 110–126. https://doi.org/10.1016/j.chemgeo.2016.01.002.
Stampfli, G. M., & Marthaler, M. (1990). Divergent and convergent margins in the North-Western Alps: Confrontation to actualistic models. *Geodinamica Acta, 4,* 159–184. https://doi.org/10.1080/09853111.1990.11105208.
Stampfli, G. M., Mosar, J., Marquer, D., Marchant, R., Baudin, T., & Borel, G. (1998). Subduction and obduction processes in the Swiss Alps. *Tectonophysics, 296,* 159–204. https://doi.org/10.1016/S0040-1951(98)00142-5.
Tartarotti, P., Festa, A., Benciolini, L., & Balestro, G. (2017). Record of Jurassic mass transport processes through the orogenic cycle: Understanding chaotic rock units in the high-pressure Zermatt-Saas ophiolite (Western Alps). *Lithosphere, 9,* 399–407. https://doi.org/10.1130/L605.1.
Thirlwall, M. F., & Anczkiewicz, R. (2004). Multidynamic isotope ratio analysis using MC-ICP-MS and the causes of secular drift in Hf, Nd and Pb isotope ratios. *International Journal of Mass Spectrometry, 235,* 59–81. https://doi.org/10.1016/j.ijms.2004.04.002.
Treves, B. E., & Harper, G. D. (1994). Exposure of serpentinites on the ocean floor: Sequence of faulting and hydrofracturing in the Northern Apennine ophicalcites. *Ofioliti, 19,* 435–466.
Tribuzio, R., Garzetti, F., Corfu, F., Tiepolo, M., & Renna, M. R. (2016). U-Pb zircon geochronology of the Ligurian ophiolites (Northern Apennine, Italy): Implications for continental breakup to slow seafloor spreading. *Tectonophysics, 666,* 220–243. https://doi.org/10.1016/j.tecto.2015.10.024.
Tricart, P., & Lemoine, M. (1983). Serpentinite oceanic bottom in south Queyras ophiolites (French Western Alps): Record of the incipient oceanic opening of the Mesozoic Ligurian Tethys. *Eclogae Geologicae Helvetiae, 76,* 611–629. https://doi.org/10.5169/seals-165379.
Trümpy, R. (1975). Penninic-Austroalpine boundary in the Swiss Alps: a presumed former continental margin and its problems. *American Journal of Science, 275*(A), 209–238.
Tucholke, B. E., Behn, M. D., Buck, W. R., & Lin, J. (2008). Role of melt supply in oceanic detachment faulting and formation of megamullions. *Geology, 36,* 455–458. https://doi.org/10.1130/G24639A.1.
Tucholke, B. E., & Lin, J. (1994). A geological model for the structure of ridge segments in slow spreading ocean crust. *Journal of Geophysical Research, 99,* 11937–11958. https://doi.org/10.1029/94JB00338.
Tucholke, B. E., Lin, J., & Kleinrock, M. C. (1998). Megamullions and mullion structure defining oceanic metamorphic core complexes on the Mid-Atlantic Ridge. *Journal of Geophysical Research, 103,* 9857–9866. https://doi.org/10.1029/98JB00167.
Ulianov, A., Müntener, O., Schaltegger, U., & Bussy, F. (2012). The data treatment dependent variability of U-Pb zircon ages obtained using monocollector, sector field, laser ablation ICPMS. *Journal of Analytical Atomic Spectrometry, 27,* 663–676. https://doi.org/10.1039/C2JA10358C.
Vitale Brovarone, A., Beltrando, M., Malavieille, J., Giuntoli, F., Tondella, E., Groppo, C., et al. (2011). Inherited Ocean-Continent Transition zones in deeply subducted terranes: Insights from Alpine Corsica. *Lithos, 124,* 273–290. https://doi.org/10.1016/j.lithos.2011.02.013.
White, W. M., & Klein, E. M. (2014). Composition of the oceanic crust. In H. D. Holland & K. K. Turekian (Eds.), *Treatise on geochemistry* (Vol. 4, pp. 457–496). Oxford: Elsivier. https://doi.org/10.1016/B978-0-08-095975-7.00315-6.
Witzig, E. (1948). *Geologische Untersuchungen in der Zone du Combin im Val des Dix (Wallis)*. Unpublished PhD thesis, Eidgenössiche Technischen Hochschule in Zürich, 62 p.
Yang, Y. H., Wu, F. Y., Yang, J. H., Chew, D. M., Xie, L. W., Chu, Z. Y., et al. (2014). Sr and Nd isotopic compositions of apatite reference materials used in U-Th-Pb geochronology. *Chemical Geology, 385,* 35–55. https://doi.org/10.1016/j.chemgeo.2014.07.012.

Publisher's Note